

Conditional Diffusion Model for Multi-Agent Dynamic Task Decomposition

Yanda Zhu¹, Yuanyang Zhu^{2†}, Daoyi Dong³, Caihua Chen^{1†}, Chunlin Chen^{4,1}

¹ School of Management and Engineering, Nanjing University, ² School of Information Management, Nanjing University

³ Australian Artificial Intelligence Institute, University of Technology Sydney,

⁴ School of Robotics and Automation, Nanjing University

yandazhu@smail.nju.edu.cn, {yuanyangzhu, chchen, clchen}@nju.edu.cn, daoyidong@gmail.com

Abstract

Task decomposition has shown promise in complex cooperative multi-agent reinforcement learning (MARL) tasks, which enables efficient hierarchical learning for long-horizon tasks in dynamic and uncertain environments. However, learning dynamic task decomposition from scratch generally requires a large number of training samples, especially exploring the large joint action space under partial observability. In this paper, we present the Conditional Diffusion Model for Dynamic Task Decomposition (CD³T), a novel two-level hierarchical MARL framework designed to automatically infer subtask and coordination patterns. The high-level policy learns subtask representation to generate a subtask selection strategy based on subtask effects. To capture the effects of subtasks on the environment, CD³T predicts the next observation and reward using a conditional diffusion model. At the low level, agents collaboratively learn and share specialized skills within their assigned subtasks. Moreover, the learned subtask representation is also used as additional semantic information in a multi-head attention mixing network to enhance value decomposition and provide an efficient reasoning bridge between individual and joint value functions. Experimental results on various benchmarks demonstrate that CD³T achieves better performance than existing baselines.

Introduction

Cooperative multi-agent reinforcement learning (MARL) has achieved great improvements and holds great promise for real-world challenging problems, such as sensor networks (Zhang and Lesser 2011), coordination of robot swarms (Hüttenrauch, Šošić, and Neumann 2017), and autonomous vehicles (Pham et al. 2018). Learning effective control policies under partial observation for coordinating such systems remains challenging. The centralized training with decentralized execution (CTDE) paradigm (Oliehoek, Spaan, and Vlassis 2008; Kraemer and Banerjee 2016) alleviates partial observability yet struggles with the exponential growth of the joint action-observation space as agent numbers increase, which makes exploration of valuable states rare and coordination difficult.

To deal with uncertainty and adapt to the dynamics of an environment, all agents learn and share a decentralized pol-

icy network under the CTDE framework. Memory-based architectures, such as recurrent neural networks (RNNs), long short-term memory (LSTM) (Hochreiter and Schmidhuber 1997), and gated recurrent units (GRUs), help agents to capture long-term dependencies in their action-observation history (Sunehag et al. 2018; Rashid et al. 2018; Son et al. 2019; Wang et al. 2021a; Liu et al. 2025). Recent transformer-based methods have shown superior performance by modeling both long- and short-term dependencies, offering a powerful solution to partial observability (Parisotto et al. 2020; Yang et al. 2022b; Wen et al. 2022). However, parameter sharing among agents can lead to similar behavior, hindering diversity. The challenge is to balance agent specialization and dynamic sharing to promote cooperation (Christianos et al. 2021).

A natural solution to this challenge is decomposing complex tasks into subtasks (Butler 2011). This decomposition not only simplifies the task but also allows agents to focus on solving specific subtasks, which can reduce the complexity of the action-observation space and enhance overall learning efficiency. Building on this idea, recent research has explored the integration of roles and skills into MARL. In the learning of roles (Wang et al. 2020a, 2021b; Li et al. 2021), skills (Yang et al. 2022a; Liu et al. 2022), or groups (Zang et al. 2023), existing works generally use a simple network structure to extract action representations for agents and may neglect fully considering the dynamic interactions among agents and the environment. The representational capacity of such a setting poses a bottleneck when trying to learn distinct latent representations for all subtasks.

Diffusion Models (Ho, Jain, and Abbeel 2020; Sohl-Dickstein et al. 2015a), a novel class of generative models known for their impressive performance in image generation tasks, offer a promising avenue to address such challenges. These models are well-suited for handling the stochasticity inherent in complex environments due to their ability to model stochastic processes through iterative denoising. Furthermore, since the spaces of histories and states in MARL are often continuous and high-dimensional, diffusion models are particularly effective because of their robust representational capacity in expansive spaces. These benefits of the diffusion model stimulate our thinking in MARL domains, i.e., *can we harness modern generative models, such as diffusion models, trained on offline data and capture useful la-*

[†]Corresponding author: Yuanyang Zhu and Caihua Chen.
Copyright © 2026, Association for the Advancement of Artificial Intelligence (www.aaai.org). All rights reserved.

tent representation that facilitates online MARL?

To explore this, we propose the Conditional Diffusion Model for Dynamic Task Decomposition CD³T. To reflect the potential characters of agents and subtasks, a set of action representations is used as the input conditioned on observations and actions of agents, while the reward of the environment and the next observations are used as the output. With this representation, we can derive subtasks by clustering and devise a subtask selection mechanism that assigns an agent to a subtask. Due to characters encoded in the subtask representation, this mechanism could select and share proper skills for agents based on parameter sharing. Benefit from the powerful representational capacity of the diffusion model, CD³T not only owns a better ability to model stochastic processes through the iterative denoising inductive bias but also learns distinguishable subtasks to explore the environment. Inspired by recent works addressing spurious correlations between global states and joint values (Li et al. 2022; Wang et al. 2023; Liu, Zhu, and Chen 2023), we incorporate subtask representations with global state information to better estimate credit assignment.

We evaluate CD³T across a range of benchmarks, including Level-based Foraging (LBF), StarCraft Multi-Agent Challenge (SMAC) (Samvelyan et al. 2019), and SMACv2 (Ellis et al. 2023). The results show that our CD³T improves the performance on SMAC compared to the baselines, especially on *Hard* and *Super Hard* scenarios. Ablation studies confirm the efficacy of task decomposition and credit assignment design, and visualizations illustrate meaningful dynamic task decompositions and cooperation.

Preliminaries

Our work focuses on a fully cooperative multi-agent task with only partial observation for each agent, which typically is modeled as a decentralized partially observable Markov decision process (Dec-POMDP) (Oliehoek and Amato 2016) and described with the tuple $\mathcal{M} = \langle \mathcal{I}, \mathcal{S}, \mathcal{A}, P, R, \Omega, O, \gamma \rangle$. At each time step, each agent $i \in \mathcal{I}$ receives an observation $o_i \in \Omega$, drawn from the observation function $O(s, i)$, where $s \in \mathcal{S}$ is the global state of the environment, and selects an action $a_i \in \mathcal{A}$, producing a joint action $\mathbf{a} = (a_1, \dots, a_n)$. This joint action would lead to the next state s' according to the state transition function $P(s'|s)$, and all agents would receive a shared team reward $r = R(s, \mathbf{a})$. We use $\tau \in \mathcal{T} \equiv (\Omega \times \mathcal{A})^*$ to denote the joint action-observation history, where $\tau = (\tau_1, \dots, \tau_n)$, and $\tau_i = (o_i^1, a_i^1, \dots, o_i^{t-1}, a_i^{t-1}, o_i^t)$ represents the trajectory of agent i . The target is to find the optimal joint policy $\pi(\mathbf{a}|\tau)$ that maximizes the discounted return, defined as $Q^\pi(\tau, \mathbf{a}) = \mathbb{E}[\sum_{t=0}^{\infty} \gamma^t R(s_t, \mathbf{a}_t) | s_0 = s, \mathbf{a}_0 = \mathbf{a}, \pi]$, where $\gamma \in [0, 1]$ is the discount factor.

Unlike recent MARL works (Sunehag et al. 2018; Rashid et al. 2018; Son et al. 2019; Wang et al. 2021a), we propose to decompose a fully cooperative multi-agent task into subtasks and present the definition of subtasks in the following.

Definition 1 (Subtasks). *Given a cooperative task $\mathcal{M} = \langle \mathcal{I}, \mathcal{S}, \mathcal{A}, P, R, \Omega, O, \gamma \rangle$, we assume there exists a set of g subtasks, denoted as $\Phi = \{\phi^1, \phi^2, \dots, \phi^g\}$, where $g \in \mathbb{N}^+$ is unknown and considered as a tunable hyperparameter. Each subtask is expressed as a tuple $\langle \mathcal{M}_{\phi^j}, \pi_{\phi^j} \rangle$, where $j \in \{1, 2, \dots, g\}$ is the identity of subtask, $\mathcal{M}_{\phi^j} = \langle \mathcal{I}_{\phi^j}, \mathcal{S}, \mathcal{A}_{\phi^j}, P, R, \Omega_{\phi^j}, O, \gamma \rangle$ and $\pi_{\phi^j} : \mathcal{T} \times \mathcal{A}_{\phi^j} \rightarrow [0, 1]$. \mathcal{I}_{ϕ^j} is the set of agents assigned to subtask ϕ^j and each agent can only select one subtask to solve at each timestep, i.e., $\mathcal{I}_{\phi^j} \subset \mathcal{I}$, $\cup_{\phi^j} \mathcal{I}_{\phi^j} = \mathcal{I}$ and $\mathcal{I}_{\phi^j} \cap \mathcal{I}_{\phi^k} = \emptyset$ if $j \neq k$. \mathcal{A}_{ϕ^j} is the action space of the subtask, $\mathcal{A}_{\phi^j} \subset \mathcal{A}$, $\cup_{\phi^j} \mathcal{A}_{\phi^j} = \mathcal{A}$, but we allow action spaces of different subtasks to overlap: $|\mathcal{A}_{\phi^j} \cap \mathcal{A}_{\phi^k}| \geq 0$ if $j \neq k$. Each agent $i \in \mathcal{I}_{\phi^j}$ shares the policy parameters of π_{ϕ^j} .*

With the set of subtasks Φ defined, each agent $i_{\phi^j} \in \mathcal{I}_{\phi^j}$ is assigned subtask ϕ^j through a shared subtask selector. This enables the learning of subtask-specific policies $\pi_{\phi^j} : \mathcal{T} \times \mathcal{A}_{\phi^j}$ for each subtask. Our objective is to learn the optimal set of subtasks Φ^* that maximizes the expected global return

$$Q_{tot}^\Phi(\tau, \mathbf{a}) = \mathbb{E}_{s_{1:\infty}, \mathbf{a}_{1:\infty}} [\sum_{t=0}^{\infty} \gamma^t r_t | s_0 = s, \mathbf{a}_0 = \mathbf{a}, \Phi].$$

Method

Our solution for multi-agent dynamic task decomposition is illustrated in *Fig. 1*. We begin by describing how to construct action semantic representations that enable the decomposition of multi-agent tasks. Next, we explain how the representations are leveraged to generate subtasks. Based on the generated subtasks and their corresponding latent representations, we introduce a hierarchical architecture consisting of a subtask selector and a set of subtask policies. Finally, we detail the training objective and inference strategy for both the subtask selector and the subtask policies.

Action Representation Learning via Diffusion

The latent action representations are designed to induce diverse subtasks with distinct responsibilities, capturing characteristic agent behaviors for more appropriate subtask selection. While this design allows CD³T to adapt to dynamic environments, it may lead to rapid subtask shifts and instability during learning. Moreover, if the induced subtasks are overly similar, decomposition becomes ineffective. Therefore, two key challenges arise: 1) ensuring temporal stability to maintain adaptability, and 2) enhancing subtask diversity through efficient modeling.

To this end, we first construct the action encoder component to map the one-hot action a_i of agent i to the d -dimensional representation z_{a_i} , which serves as unmodified examples z_0 . Then the UNet backbone with cross-attention is employed as a flexible feature extractor in the denoising network $\epsilon_{\theta_d}(z_k, k, o_i, a_{-i})$ to recover z_{a_i} from Gaussian noise $\epsilon \sim \mathcal{N}(0, I)$ conditioned on corresponding o_i and a_{-i} . Following the simplified objective (Ho, Jain, and Abbeel 2020), we formulate a learning objective for action representations via the conditional diffusion model parameterized by θ_d , which is trained by minimizing the loss function:

$$\mathcal{L}_d(\theta_d) = \mathbb{E}_{\epsilon \sim \mathcal{N}(0, I), (o, a) \sim \mathcal{D}} [\|\epsilon - \epsilon_{\theta_d}(z_k, k, o_i, a_{-i})\|^2], \quad (1)$$

where \mathcal{D} denotes the replay buffer, k is the diffusion iteration uniformly sampled from $\{1, 2, \dots, K\}$ and z_k is the noisy

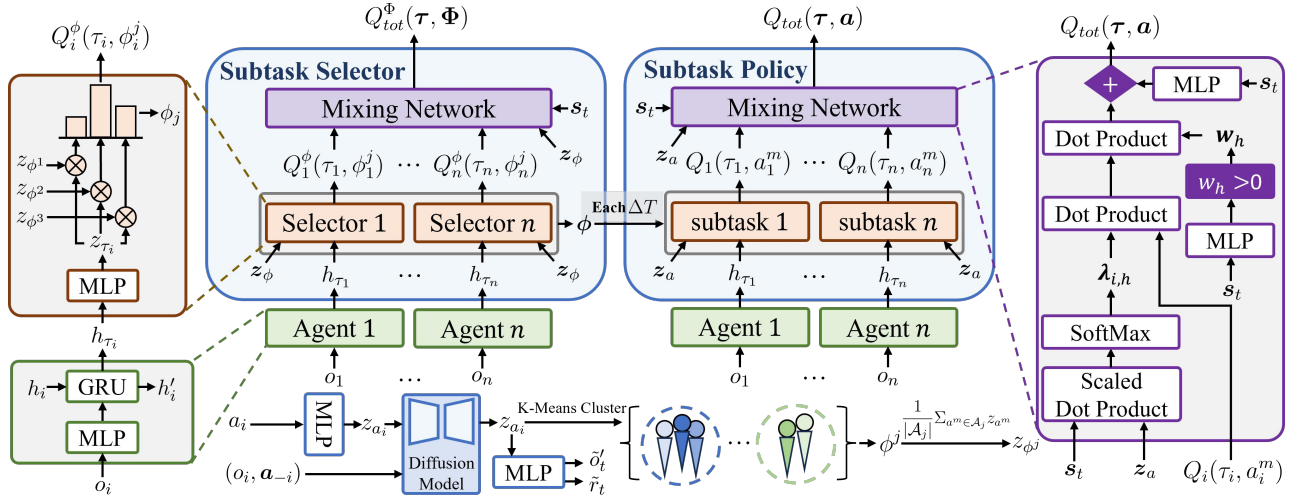


Figure 1: The overall framework of CD³T. We first derive a latent action representation z_{a_i} for each agent from its action space, conditioned on its local observation o_i and other agents’ one-hot actions a_{-i} , to pretrain a diffusion model. Latent representations are then clustered to define subtask-specific action spaces. The subtask selector and subtask policy share the same architecture with different parameters. At every ΔT steps, the selector assigns a subtask to each agent and estimates the joint Q-value Q_{tot}^{ϕ} using the global state s_t and subtask representation z_{ϕ} , while the subtask policy computes Q_{tot} with s_t and the action representation z_a .

version of z_0 . Here, o_i denotes the observation of agent i , while a_{-i} denotes the joint actions of all other agents. The detailed derivation can be found in Appendix A.

Action semantics, where different actions have varying effects on other agents, should influence the environment or their private properties. To further extract the influence of an action through the induced reward and the change in local observations, we leverage the action representations generated by the diffusion model to predict the next observations o'_i and global reward r based on o_i and a_{-i} . The prediction objective can be further rewritten as a loss function:

$$\mathcal{L}_p(\theta) = \mathbb{E}_{(o, a, r, o') \sim \mathcal{D}} \left[\sum_i \|f_{do}(z_{a_i}, o_i, a_{-i}) - o'_i\|_2^2 + \lambda_{dr} \sum_i (f_{dr}(z_{a_i}, o_i, a_{-i}) - r)^2 \right], \quad (2)$$

where f_{do} and f_{dr} are predictors of observations and global rewards, respectively, and λ_{dr} is a scaling factor. Here, the summation covers all agents, and the whole action representation learning is parameterized by θ . Thus, the objective for action representation learning combines the prediction loss and the diffusion model loss with a scaling factor η_d :

$$\mathcal{L}(\theta) = \mathcal{L}_p(\theta) + \eta_d \mathcal{L}_d(\theta_d). \quad (3)$$

The current formulation does not explicitly enforce subtask specialization, which is essential for ensuring behavioral diversity across different subtasks. Prior approaches typically encourage specialization via explicit regularization techniques (Christianos et al. 2021; Wang et al. 2020a). In contrast, we utilize the diffusion model as a flexible feature extractor and enhance its UNet backbone with cross-attention to generate action representations that capture multimodal distributions. This property naturally induces subtask diversity without additional regularization.

Subtask Dynamic Decomposition

The action representation plays a critical role in assigning agents to the most suitable subtasks, where agents dealing with the same subtask share their learning of specific abilities. Considering that an agent’s subtask history reflects not only its behavioral history but is also task-independent, we perform k -means clustering over these action representations to decompose the task into a finite set of subtasks after sampling and learning for the initial $50K$ timesteps of the overall training process. Given the action representations of subtask ϕ^j , the subtask representation z_{ϕ^j} can be derived as $z_{\phi^j} = \frac{1}{|\mathcal{A}_j|} \sum_{a^m \in \mathcal{A}_j} z_{a^m}$, where \mathcal{A}_j represents the decomposed action space of the subtask ϕ^j and a^m denotes actions in this restricted space. With a hierarchical network consisting of the subtask selector and the subtask policies, subtask representations can be used to assign the most suitable subtask to an agent over a specific time interval ΔT . Similarly, an MLP layer and a shared GRU layer network are shared by all agents to obtain the historical information of the agent’s local observations and actions, which is parameterized by $\theta_{\tau_{\phi}}$ and compiles it into a vector h for our subtask selection.

When selecting subtasks every ΔT timesteps, the subtask selector encodes the historical information h_{τ_i} of each agent into the hidden layer variable $z_{\tau} \in \mathbb{R}^d$ with a ξ_{ϕ} -parameterized encoder $f_{\phi}(\cdot; \xi_{\phi})$. Then it is used to estimate the expected return of agent i in subtask ϕ^j with the hidden layer representation of each subtask space $Q_i^{\phi}(\tau_i, \phi^j) = z_{\tau_i}^T z_{\phi^j}$. The subtask space corresponding to the maximum Q-value is assigned to each agent. In the next ΔT time step, each agent learns its policy in the restricted subtask space.

Learning Decomposition with Credit Assignment

The global state s in multi-agent systems contains rich information, yet only a subset is relevant to individual decision-

making. To extract meaningful abstractions without relying on expert knowledge, we follow (Li et al. 2022; Liu, Zhu, and Chen 2023; Xu et al. 2025) and mitigate spurious correlations between s and Q_{tot} by leveraging agents’ local histories τ_i in partially observable settings. To improve decomposition accuracy and credit assignment, we introduce an intervention-based adjustment function during training, which adheres to the Individual-Global-Maximum (IGM) principle in Appendix B.

Specifically, the credit $\lambda_{h,i}^\phi$ for subtask selector is computed with the subtask representation z_ϕ and the global state s through a dot-product attention as

$$\lambda_{h,i}^\phi = \frac{\exp((\mathbf{w}_{z_\phi} z_\phi)^\top \text{ReLU}(\mathbf{w}_s s))}{\sum_{i=1}^N \exp((\mathbf{w}_{z_\phi} z_\phi)^\top \text{ReLU}(\mathbf{w}_s s))}, \quad (4)$$

where $\mathbf{w}_s, \mathbf{w}_{z_\phi}$ are learnable weight matrices, and ReLU is the element-wise rectified-linear activation. $\lambda_{h,i}^\phi$ is positive with softmax operation to ensure monotonicity and h is the number of attention heads. The softmax ensures each $\lambda_{h,i}^\phi$ is positive and that $\sum_i \lambda_{h,i}^\phi = 1$. Then the joint action function Q_{tot}^Φ of the subtask selector can be estimated as

$$Q_{tot}^\Phi = c_\phi(s) + \sum_{h=1}^H w_h^\phi \sum_{i=1}^N \lambda_{h,i}^\phi Q_i^{\phi^j}(\tau_i, a_i^m), \quad (5)$$

where $c_\phi(s)$ is learned by a neural network with the global state s as the input. The joint action function Q_{tot}^Φ of the subtask selector can be optimized by minimizing TD loss:

$$\mathcal{L}_{ss}(\theta_{\tau_\phi}, \xi_\phi) = \mathbb{E}_{\mathcal{D}} \left[\left(\sum_{\Delta t=0}^{\Delta T-1} r_{t+\Delta t} + \gamma \max_{\Phi'} \bar{Q}_{tot}^\Phi(s_{t+\Delta T}, \Phi') - Q_{tot}^\Phi(s_t, \Phi_t) \right)^2 \right], \quad (6)$$

where ξ_ϕ denotes the parameters of the mixing network, $\Phi = \langle \phi^1, \phi^2, \dots, \phi^N \rangle$ is the joint subtask of all agents, and the expectation is taken over mini-batches sampled uniformly from the replay buffer \mathcal{D} .

During the timestep of ΔT , each agent follows the subtask assigned by the high-level selector. When the agent is assigned to the corresponding subtask, it selects its action in the action space of the subtask. Therefore, each subtask has a corresponding policy $\pi_{\phi^j} : \mathcal{T} \times \mathcal{A}_{\phi^j} \rightarrow [0, 1]$, which is defined in the restricted subtask action space and updates such a policy network. To take full advantage of the action representation of the corresponding subtask space, we also use the mechanism to compute the joint function Q_{tot} . Here, we use the shared MLP layer and GRU layer parameterized by θ_τ in the same way to compile the local action-observation information history τ into a vector h_τ . For each subtask policy, we use a fully connected network $f_{\phi^j}(h_\tau; \zeta_\phi)$ parameterized by ζ_ϕ to represent it. Thus we estimate the individual value of agent i by choosing a primitive action a_i^m as $Q_i(\tau_i, a_i^m) = z_{\tau_i}^T z_{a_i^m}$.

Similar to the value function factorization of the subtask selector, the action representation z_a and the global state s are still fed into the intervention function to estimate credits. Here, the action representations are restricted in the action

space of the subtasks assigned to the agent, rather than the subtask representations in the subtask selector, so the credit $\lambda_{h,i}$ for the subtask policy is computed as

$$\lambda_{h,i} = \frac{\exp((\mathbf{w}_{z_a} z_a)^\top \text{ReLU}(\mathbf{w}_s s))}{\sum_{i=1}^N \exp((\mathbf{w}_{z_a} z_a)^\top \text{ReLU}(\mathbf{w}_s s))}, \quad (7)$$

where $\mathbf{w}_s, \mathbf{w}_{z_a}$ are the learnable parameters, and ReLU is the activation function. $\lambda_{h,i}$ is positive with softmax operation to ensure monotonicity and h is the number of attention heads. The joint value function of the subtask policy is predicted based on the credits and factorized Q-values

$$Q_{tot} = c(s) + \sum_{h=1}^H w_h \sum_{i=1}^N \lambda_{h,i} Q_i(\tau_i, a_i^m), \quad (8)$$

where $c(s)$ is learned by a neural network with the global state s as the input. The formulation gives the TD loss for subtask policies:

$$\mathcal{L}_s(\theta_\tau, \xi) = \mathbb{E}_{\mathcal{D}} [(r + \gamma \max_{\mathbf{a}'} \bar{Q}_{tot}(s', \mathbf{a}') - Q_{tot}(s, \mathbf{a}))^2], \quad (9)$$

where the parameters of the mixing network are denoted by ξ and \bar{Q}_{tot} is a target network. Training samples are drawn uniformly from the same replay buffer \mathcal{D} used for the high-level selector. Under the CTDE paradigm, the selector, subtask policies, and individual utility networks are used jointly at execution time, but only local information is required for each agent to act. Pseudocode for the complete CD³T algorithm is given in Appendix C.

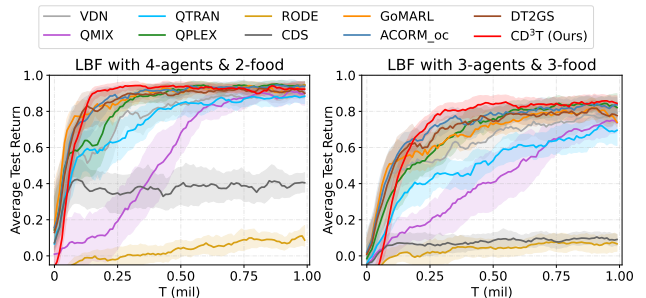


Figure 2: Performance comparison with baselines on LBF.

Experiments

We evaluate CD³T on three challenging benchmarks, including LBF (Christanios, Schäfer, and Albrecht 2020), SMAC (Samvelyan et al. 2019) and SMACv2 (Ellis et al. 2023). The baselines we select are five classic value-decomposition methods (VDN (Sunehag et al. 2018), QMIX (Rashid et al. 2020), QTRAN (Son et al. 2019), QPLEX (Wang et al. 2021a), and CDS (Li et al. 2021)), and four subtask-related methods (RODE (Wang et al. 2021b), GoMARL (Zang et al. 2023), ACORM (Hu et al. 2024) and DT2GS (Tian et al. 2023)). ACORM performs k -means clustering at each timestep to obtain commendable results, which undoubtedly imposes a substantial computational burden. Therefore, to improve efficiency and maintain consistency with our algorithm, we likewise apply clustering for

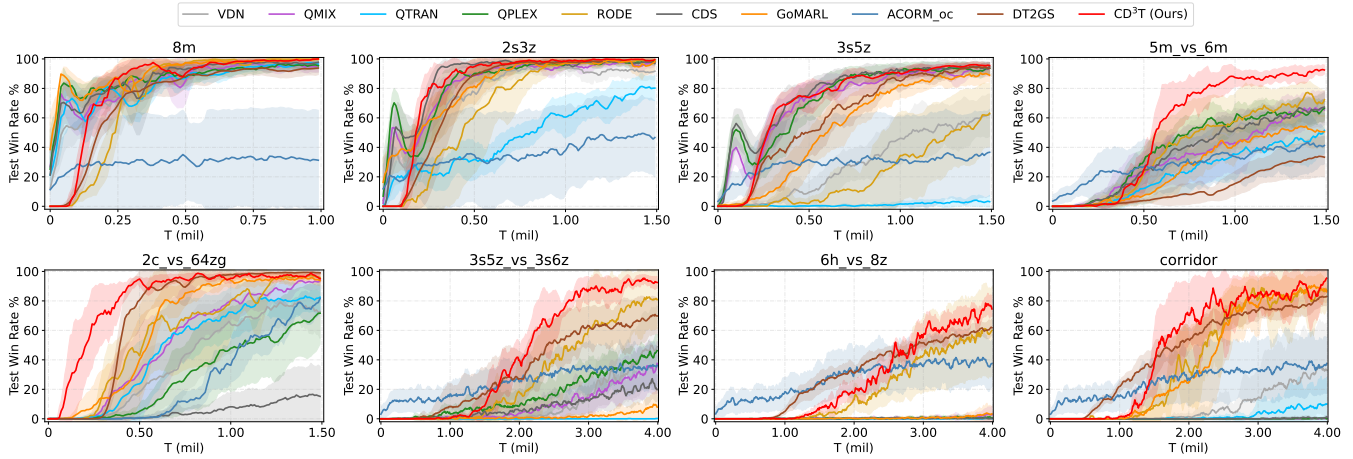


Figure 3: Performance comparison with baselines on *easy*, *hard*, and *super hard* scenarios.

ACORM only once at 50K timesteps. We use ‘‘ACORM_oc’’ to represent ACORM with once clustering in our experiments. The implementation details of all algorithms are provided in Appendix D, along with benchmarks and discussions on training time and scalability. All learning curves report the mean \pm standard deviation over five random seeds.

Performance on LBF

We first conduct experiments on two constructed LBF tasks to assess the performance of different algorithms under two distinct settings. Fig. 2 illustrates a comprehensive comparison of performance against baselines on two specially crafted LBF tasks. Our approach shows competitive performance across LBF tasks, demonstrating its flexibility and effectiveness on both scenarios. The failure of CDS and RODE could originate from the inability of its heterogeneous agents to effectively explore and develop collaborative strategies. In contrast, VDN, QMIX, and QTRAN require more steps to uncover more refined policies, suggesting that they may struggle with the inherent limitations in solving spurious relationships between credit assignments and decomposed Q-values. QPLEX receives a lower return compared to CD³T between 0.1M and 0.6M timesteps, potentially necessitating additional time for exploration due to its complex value decomposition design. CD³T achieves slightly higher performance than GoMARL and ACORM, which implies that in terms of semantic representation, the action representation may have superiority over both group-based information and role representation. The marginally inferior performance of DT2GS compared to CD³T further substantiates that enhancing the generalization of subtasks inevitably entails a trade-off with performance on single tasks.

Performance on SMAC

To further evaluate CD³T, we benchmark it on the more challenging SMAC benchmark, which is a testbed commonly used for MARL algorithms. We compare CD³T with other baselines on 8 different scenarios, including *easy*, *hard*, and *super hard* scenarios. The details of these scenarios can be found in Appendix D.

The experimental results for different scenarios are shown in Fig. 3. As we can see, CD³T yields almost the highest win rate on all scenarios, especially on the *super hard* tasks. QTRAN performs poorly on almost all scenarios due to its soft constraints involving two ℓ_2 -penalty terms. Although QPLEX behaves well on easy scenarios, resulting in its tendency to fall into local optima, its performance decreases on hard scenarios. Both VDN and QMIX can achieve satisfactory performance on some *easy* or *hard* maps, i.e., 8m, 2s3z, and 5m_vs_6m, but they fail to cope with the tasks well on *super hard* maps. It should result from the fact that the super-hard task needs more efficient exploration to learn cooperation skills. RODE fails to learn efficient policies for subtasks, which implies that its reliance solely on the simple MLP structure hinders the accurate learning of role semantics. CDS fails to learn efficient policies since it may require more steps to explore, which celebrates diversity among agents, especially on the map corridor and 6h_vs_8z. GoMARL attains comparable performance with CD³T on part of easy and hard maps but underperforms on two *super hard* maps, possibly owing that the automatic grouping method primarily places excessive emphasis on the relative contribution of each agent to the entire group while ignoring the mutual contributions among agents within the group. ACORM achieves strong early learning, yet once per-step clustering is removed (ACORM-oc), performance collapses on nearly all maps, implying that its contrastive role representations rely heavily on continuous reclustering. One possible explanation for the consistently suboptimal performance of DT2GS is its excessive emphasis on generalization across a limited set of tasks. Overall, our approach achieves impressive performance across all scenarios, which validates the advantages of CD³T with its attentive design. Additional experiments on SMACv2 in the Appendix E further confirm the effectiveness of CD³T.

Ablation Studies

To quantify the contribution of each component, we perform three ablations and address the following questions: (a) How does the diffusion model enhance subtask representa-

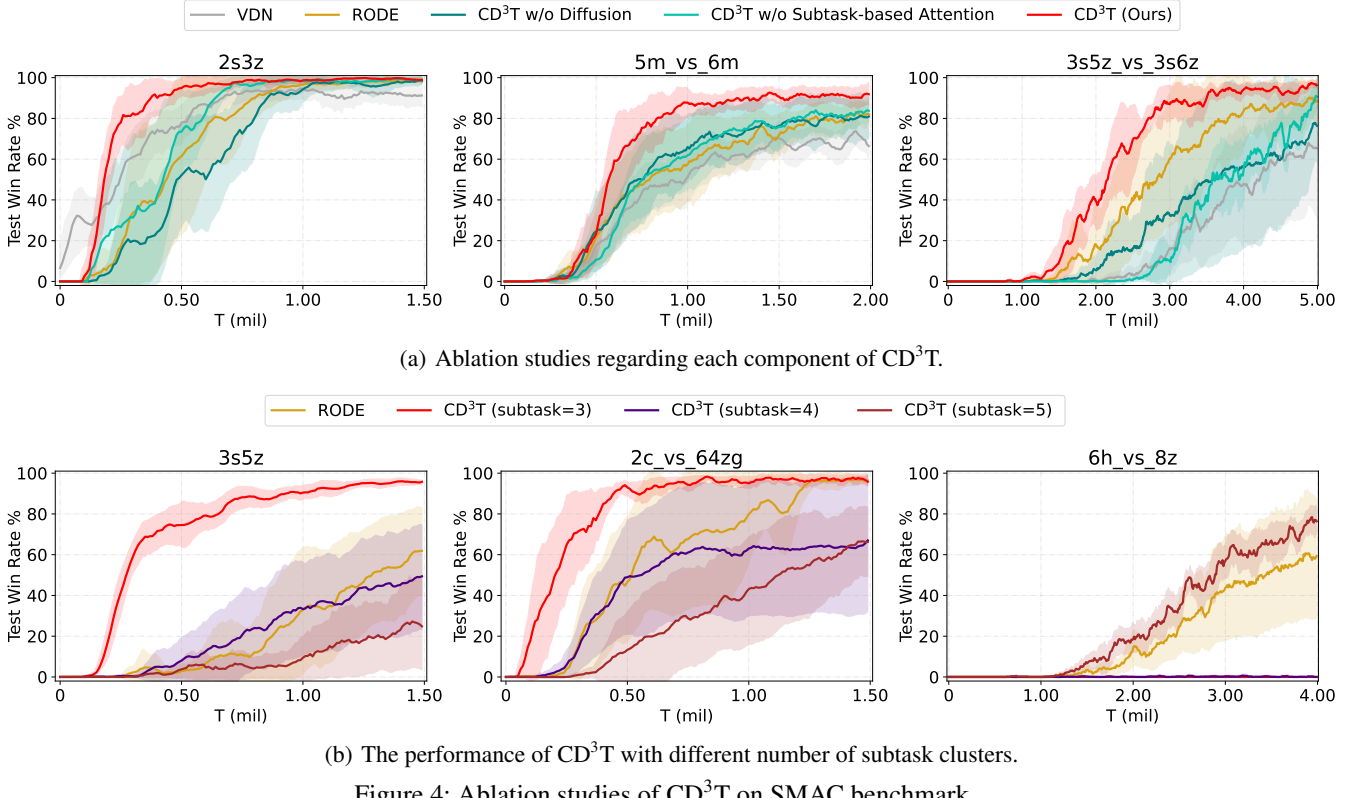


Figure 4: Ablation studies of CD^3T on SMAC benchmark.

tion and improve overall performance? (b) What role does the attention mechanism leveraging subtask representation play in credit assignment? (c) Does the number of subtasks affect the capability of the model? To test components (a), we replace the diffusion model with a vanilla MLP structure and denote it as CD^3T w/o diffusion. For (b), we replace the subtask-based attention mechanism in our mixing network, which is substituted with the QMIX method, and denote it as CD^3T w/o Subtask-based Attention. To test component (c), we test it with the number of subtasks formed during clustering, named CD^3T (subtask=3). Considering an excessive number of subtasks could not affect the performance for the finite action space, we set the number of subtasks to $3 \leq \text{subtasks} \leq 5$.

The results on three scenarios with different difficulties are shown in Fig. 4. CD^3T w/o diffusion attains the lowest win rates on all maps—particularly the hard and super hard ones—highlighting the critical role of diffusion-based subtask representations in high-dimensional state-action spaces. Especially on the hard and super hard maps, it becomes clear that CD^3T achieves a larger margin than replacing the diffusion with a simple MLP. The reason is that associating subtask policy with its proven powerful representational capacity in such expansive spaces benefits the performance in complex tasks. CD^3T w/o Subtask-based Attention is lower than that of CD^3T , which indicates the importance of subtask representation for estimating credits. As shown in Fig. 4(b), the performance of CD^3T consistently improves as the number of subtasks increases. Generally, moderate order terms (e.g., $\text{subtask} \leq 5$) are enough for an appropriate

trade-off between performance improvement and computation. In summary, the superior performance of CD^3T is conditioned on all parts, where it is largely due to the efficient subtask assignment representation.

Generation of Subtask Representation

To learn action representations, we collect samples and train the diffusion model for $50K$ timesteps, guided by the loss function specified in Eq. (3). The model is trained after each episode using a batch of 32 episodes. In Fig. 5, we provide an in-depth illustration of how the action representations derived from the diffusion model are strategically harnessed to enable subtask decomposition.

The corridor scenario features homogeneous agents and enemies—specifically, 6 Zealots versus 24 Zerglings—where all attack actions produce similar effects due to enemy uniformity. Owing to the scenario’s spatial symmetry, moving north or east similarly advances agents toward the enemies, while moving south or west leads them away. The trained diffusion model captures these structural regularities within the action space, as illustrated in Fig. 5(a). In Fig. 5(b), we apply PCA to project the high-dimensional action representations into a two-dimensional space, revealing clear clusters aligned with the primary action types. These clusters emerge consistently across random seeds, demonstrating that our attentive diffusion model reliably learns subtask representations that reflect the underlying action effects.

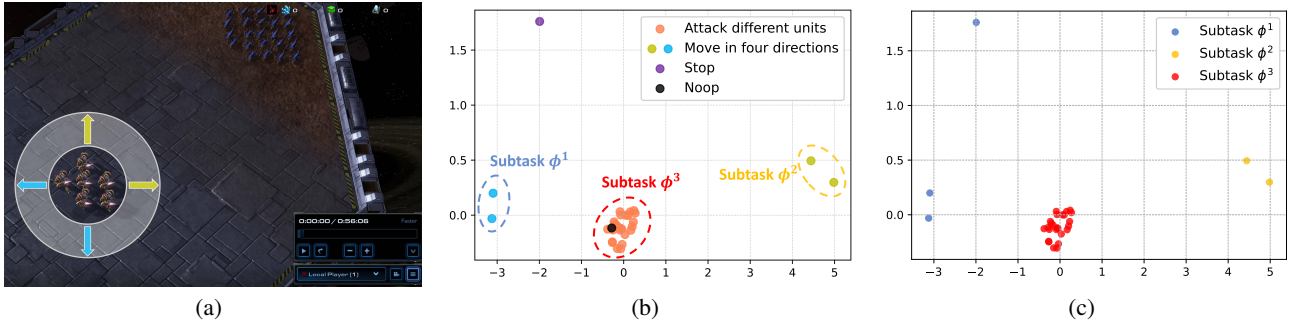


Figure 5: The process of subtask generation through subtask representations. (a) illustrates that moving northward or eastward has a comparable effect on the environment by directing agents toward the enemies, whereas moving southward or westward moves agents away. (b) depicts the distribution of action representations in a two-dimensional space after PCA projection. (c) visualizes the formation of subtasks derived from action representations following clustering.

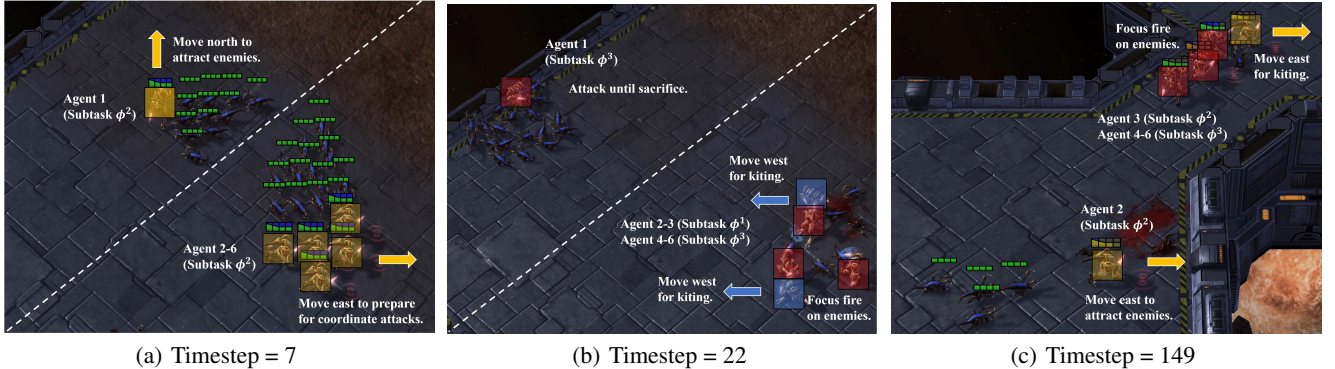


Figure 6: Visualizations of dynamic subtask selection in one episode (351 timesteps) on corridor. Blue denotes subtask ϕ^1 , yellow denotes subtask ϕ^2 , and red denotes subtask ϕ^3 . (a), (b), and (c) depict game screenshots at $t = 7$, $t = 22$, and $t = 149$, respectively.

Visualization of Dynamic Subtask Selections

To gain deeper insights into the subtask selection behavior of CD³T, we visualize the agent-wise subtask assignments across a representative episode (Fig.6) and report the corresponding selection frequencies over time (Fig.7). Additional examples are included in Appendix G.

A key observation is that direct engagement under numerical disadvantage is strategically suboptimal. As shown in Fig. 6(a), CD³T assigns subtask ϕ^2 to Agent 1 early in the episode ($t = 7$), prompting it to move northward and draw nearly half of the enemies away. This diversion enables the remaining five agents to reposition eastward for a more coordinated attack. In Fig. 6(b), Agent 1 switches to subtask ϕ^3 to engage the enemies directly until eliminated. Meanwhile, Agents 2 and 3 execute kiting behaviors under ϕ^1 , while Agents 4–6 focus fire under ϕ^3 . As the battle progresses, surviving enemies regroup in the bottom-left corner, out of sight of the Zealots. During mid-phase, CD³T reassigns subtask ϕ^2 to Agent 2 to lure a subset of enemies away from the group and disrupt their formation. Meanwhile, the remaining agents continue alternating between evasive movement and focused fire to isolate and eliminate targets.

The frequency distribution in Fig. 7 further confirms these dynamics. Subtask ϕ^2 is predominantly utilized in the early stage for diversion, followed by adaptive switching among

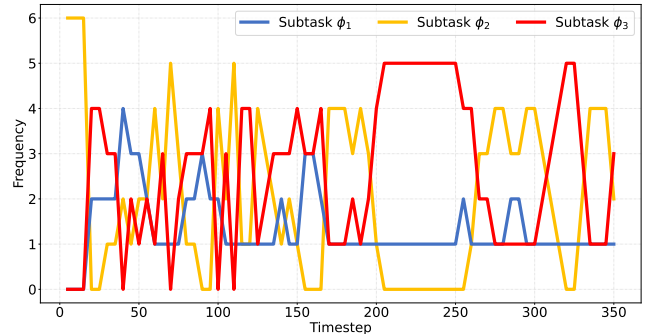


Figure 7: Demonstrates subtask selection frequencies of CD³T on corridor map in the same episode. The curve represents the number of agents assigned the corresponding subtask at the timestep.

ϕ^1 , ϕ^2 , and ϕ^3 to sustain a balanced coordination strategy involving distraction, kiting, and concentrated attack. This cyclical subtask adaptation underlines CD³T’s ability to orchestrate complex multi-agent behaviors, ultimately leading to task success.

Empirical Visualization of Action Space Reduction

Fig. 8 presents a comparative visualization of the effective action space dimensions under three methods: CD³T,

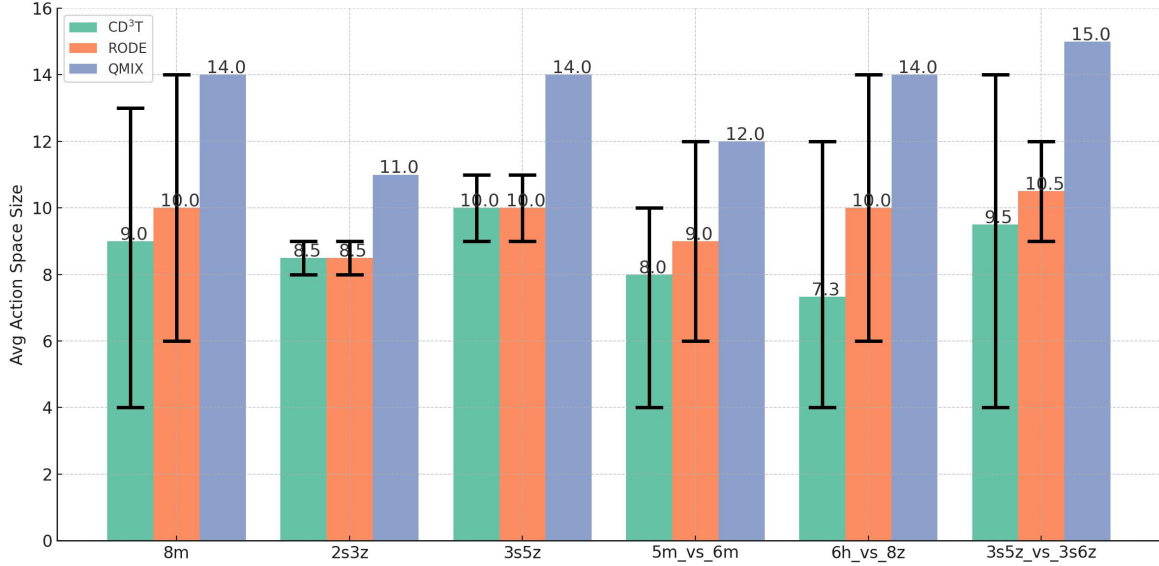


Figure 8: Average action space sizes of CD³T, RODE, and QMIX across six SMAC scenarios. Each bar denotes the mean number of available actions per method, while the error bars capture variation across roles or agents, ranging from the minimum to the maximum number of available actions. QMIX takes actions over the full action space without any form of masking, and thus does not produce variation.

RODE, and QMIX. CD³T consistently achieves a more compact action space across diverse scenarios, as reflected in its lower average dimensionality and tighter confidence intervals. This suggests that its fine-grained subtask decomposition enables each sub-policy to operate within a task-relevant, reduced action set. By comparison, QMIX does not incorporate any subtask or role abstraction, and thus always utilizes the full action space. Its action dimensionality remains fixed across scenarios, which may limit its adaptability to varying task complexity or coordination requirements. In relatively simple environments such as 8m, 2s3z, and 3s5z, both CD³T and RODE exhibit similar action space sizes, indicating that in low-complexity settings, the benefits of explicit decomposition may be less pronounced. However, in more challenging scenarios, 5m_vs_6m, 6h_vs_8z, and 3s5z_vs_3s6z, CD³T achieves more substantial reduction. This improvement may be attributed to its explicit subtask masking mechanism, which restricts each role to a compact, specialized action subset. In contrast, RODE’s role abstraction is more implicit and does not enforce strict action sparsity, potentially resulting in less targeted compression.

These findings highlight CD³T’s ability to adaptively reduce the decision space in accordance with task complexity. By focusing each agent on a smaller, semantically meaningful set of actions, CD³T not only improves computational efficiency but also facilitates more structured and scalable coordination in challenging multi-agent environments.

Conclusions

Task decomposition is a pivotal approach to simplifying complex multi-agent tasks, yet it remains a long-standing and unresolved challenge. To address this, we proposed leveraging latent representations extracted by a diffusion

model to decompose tasks into multiple subtasks. This approach captures the relationship between subtasks and environmental dynamics more accurately. Agents are assigned to corresponding subtasks through subtask selectors, ensuring better compatibility between agents and subtasks. This compatibility enables agents to learn policies more efficiently in a shared learning framework. Furthermore, by clustering latent representations, similar agents can share experiences, accelerating training and enhancing overall performance. During training, the subtask-based attention mechanism in the mixing network effectively utilizes global state and semantic inference to guide the mixing of Q-values. Experimental results across three benchmarks demonstrate that our method achieves superior performance in nearly all scenarios, advancing the state of the art in MARL.

Acknowledgements

This work was supported in part by the National Natural Science Foundation of China (Nos. 72394363, 72394364 & 72394360), National Key Research and Development Program of China (2025YFA101690004), Major Science and Technology Project of Jiangsu Province under Grant BG2024041, and the Fundamental Research Funds for the Central Universities under Grant 011814380048, the China Postdoctoral Science Foundation under Grant Number 2025T180877, the Jiangsu Funding Program for Excellent Postdoctoral Talent 2025ZB267.

Impact Statements

The goal of this work is to advance the field of Machine Learning. There are no potential societal consequences of our work, none of which we feel must be specifically highlighted here.

References

Al-Emran, M. 2015. Hierarchical reinforcement learning: a survey. *International Journal of Computing and Digital Systems*, 4(2): 137–143.

Butler, E. 2011. *The Condensed Wealth of Nations*. Adam Smith Institute.

Christianos, F.; Papoudakis, G.; Rahman, M. A.; and Albrecht, S. V. 2021. Scaling multi-agent reinforcement learning with selective parameter sharing. In *Proc. Int. Conf. Mach. Learn.*, volume 139, 1989–1998.

Christianos, F.; Schäfer, L.; and Albrecht, S. 2020. Shared experience actor-critic for multi-agent reinforcement learning. In *Proc. Adv. Neural Inf. Process. Syst.*, volume 33, 10707–10717.

Daniel, C.; Neumann, G.; Kroemer, O.; and Peters, J. 2016. Hierarchical Relative Entropy Policy Search. *Journal of Machine Learning Research*, 17(93): 1–50.

Dayan, P.; and Hinton, G. E. 1992. Feudal Reinforcement Learning. In *Proc. Adv. Neural Inf. Process. Syst.*, volume 5, 271–278.

Dilokthanakul, N.; Kaplanis, C.; Pawlowski, N.; and Shanahan, M. 2019. Feature control as intrinsic motivation for hierarchical reinforcement learning. *IEEE Trans. Neural Netw. Learn. Syst.*, 30(11): 3409–3418.

Ellis, B.; Cook, J.; Moalla, S.; Samvelyan, M.; Sun, M.; Mahajan, A.; Foerster, J. N.; and Whiteson, S. 2023. SMACv2: An Improved Benchmark for Cooperative Multi-Agent Reinforcement Learning. In *Proc. Adv. Neural Inf. Process. Syst.*, volume 36.

Gupta, T.; Mahajan, A.; Peng, B.; Böhmer, W.; and Whiteson, S. 2021. UneVEN: Universal Value Exploration for Multi-Agent Reinforcement Learning. In *Proc. Int. Conf. Mach. Learn.*, volume 139, 3930–3941.

He, H.; Bai, C.; Xu, K.; Yang, Z.; Zhang, W.; Wang, D.; Zhao, B.; and Li, X. 2023. Diffusion Model is an Effective Planner and Data Synthesizer for Multi-Task Reinforcement Learning. In *Proc. Adv. Neural Inf. Process. Syst.*, volume 36, 64896–64917.

Hegde, S.; Batra, S.; Zentner, K.; and Sukhatme, G. 2023. Generating behaviorally diverse policies with latent diffusion models. In *Proc. Adv. Neural Inf. Process. Syst.*, volume 36, 7541–7554.

Ho, J.; Jain, A.; and Abbeel, P. 2020. Denoising Diffusion Probabilistic Models. In *Proc. Adv. Neural Inf. Process. Syst.*, volume 33, 6840–6851.

Hochreiter, S.; and Schmidhuber, J. 1997. Long short-term memory. *Neural Computation*, 9(8): 1735–1780.

Hu, Z.; Zhang, Z.; Li, H.; Chen, C.; Ding, H.; and Wang, Z. 2024. Attention-Guided Contrastive Role Representations for Multi-Agent Reinforcement Learning. In *Proc. Int. Conf. Learn. Represent.*

Hüttenrauch, M.; Šošić, A.; and Neumann, G. 2017. Guided deep reinforcement learning for swarm systems. *arXiv preprint arXiv:1709.06011*.

Jang, E.; Gu, S.; and Poole, B. 2017. Categorical Reparameterization with Gumbel-Softmax. In *Proc. Int. Conf. Learn. Represent.*

Janner, M.; Du, Y.; Tenenbaum, J. B.; and Levine, S. 2022. Planning with Diffusion for Flexible Behavior Synthesis. In *Proc. Int. Conf. Mach. Learn.*, volume 162, 9902–9915.

Kingma, D. P.; and Welling, M. 2014. Auto-Encoding Variational Bayes. In *Proc. Int. Conf. Learn. Represent.*

Kraemer, L.; and Banerjee, B. 2016. Multi-agent reinforcement learning as a rehearsal for decentralized planning. *Neurocomputing*, 190: 82–94.

Lee, Y.; Yang, J.; and Lim, J. J. 2020. Learning to Coordinate Manipulation Skills via Skill Behavior Diversification. In *Proc. Int. Conf. Learn. Represent.*

Li, C.; Wang, T.; Wu, C.; Zhao, Q.; Yang, J.; and Zhang, C. 2021. Celebrating Diversity in Shared Multi-Agent Reinforcement Learning. In *Proc. Adv. Neural Inf. Process. Syst.*, volume 34, 20888–20900.

Li, J.; Kuang, K.; Wang, B.; Liu, F.; Chen, L.; Fan, C.; Wu, F.; and Xiao, J. 2022. Deconfounded value decomposition for multi-agent reinforcement learning. In *Proc. Int. Conf. Mach. Learn.*, volume 162, 12843–12856.

Liu, Y.; Li, Y.; Xu, X.; Dou, Y.; and Liu, D. 2022. Heterogeneous Skill Learning for Multi-agent Tasks. In *Proc. Adv. Neural Inf. Process. Syst.*, volume 35, 26412–26425.

Liu, Z.; Zhu, Y.; and Chen, C. 2023. NA²Q: Neural Attention Additive Model for Interpretable Multi-Agent Q-Learning. In *Proc. Int. Conf. Mach. Learn.*, volume 202, 22539–22558. PMLR.

Liu, Z.; Zhu, Y.; Wang, Z.; Gao, Y.; and Chen, C. 2025. MIXRTs: Toward interpretable multi-agent reinforcement learning via mixing recurrent soft decision trees. *IEEE Trans. Pattern Anal. Mach. Intell.*, 47(5): 4090–4107.

Lu, C.; Ball, P.; Teh, Y. W.; and Parker-Holder, J. 2023. Synthetic Experience Replay. In *Proc. Adv. Neural Inf. Process. Syst.*, volume 36.

Nair, S.; and Finn, C. 2020. Hierarchical Foresight: Self-Supervised Learning of Long-Horizon Tasks via Visual Subgoal Generation. In *Proc. Int. Conf. Learn. Represent.*

Oliehoek, F. A.; and Amato, C. 2016. *A Concise Introduction to Decentralized POMDPs*. Springer.

Oliehoek, F. A.; Spaan, M. T.; and Vlassis, N. 2008. Optimal and approximate Q-value functions for decentralized POMDPs. *J. Artif. Intell. Res.*, 32: 289–353.

Parisotto, E.; Song, F.; Rae, J.; Pascanu, R.; Gulcehre, C.; Jayakumar, S.; Jaderberg, M.; Lopez Kaufman, R.; Clark, A.; Noury, S.; Botvinick, M.; Heess, N.; and Hadsell, R. 2020. Stabilizing Transformers for Reinforcement Learning. In *Proc. Int. Conf. Mach. Learn.*, volume 119, 7487–7498.

Pham, H. X.; La, H. M.; Feil-Seifer, D.; and Nefian, A. 2018. Cooperative and distributed reinforcement learning of drones for field coverage. *arXiv preprint arXiv:1803.07250*.

Rashid, T.; Farquhar, G.; Peng, B.; and Whiteson, S. 2020. Weighted QMIX: Expanding Monotonic Value Function

Factorisation for Deep Multi-Agent Reinforcement Learning. In *Proc. Adv. Neural Inf. Process. Syst.*, volume 33, 10199–10210.

Rashid, T.; Samvelyan, M.; Schroeder, C.; Farquhar, G.; Foerster, J.; and Whiteson, S. 2018. QMIX: Monotonic Value Function Factorisation for Deep Multi-Agent Reinforcement Learning. In *Proc. Int. Conf. Mach. Learn.*, volume 80, 4295–4304.

Samvelyan, M.; Rashid, T.; de Witt, C. S.; Farquhar, G.; Nardelli, N.; Rudner, T. G.; Hung, C.-M.; Torr, P. H.; Foerster, J.; and Whiteson, S. 2019. The StarCraft Multi-Agent Challenge. In *Proc. Int. Conf. Auto. Agents Multiagent Syst.*, 2186–2188.

Sharma, A.; Gu, S.; Levine, S.; Kumar, V.; and Hausman, K. 2020. Dynamics-Aware Unsupervised Discovery of Skills. In *Proc. Int. Conf. Learn. Represent.*

Sohl-Dickstein, J.; Weiss, E.; Maheswaranathan, N.; and Ganguli, S. 2015a. Deep Unsupervised Learning using Nonequilibrium Thermodynamics. In *Proc. Int. Conf. Mach. Learn.*, volume 37, 2256–2265.

Sohl-Dickstein, J.; Weiss, E. A.; Maheswaranathan, N.; and Ganguli, S. 2015b. Deep Unsupervised Learning using Nonequilibrium Thermodynamics. In *Proc. Int. Conf. Mach. Learn.*, volume 37, 2256–2265.

Son, K.; Kim, D.; Kang, W. J.; Hostallero, D.; and Yi, Y. 2019. QTRAN: Learning to Factorize with Transformation for Cooperative Multi-Agent Reinforcement Learning. In *Proc. Int. Conf. Mach. Learn.*, volume 97, 5887–5896.

Song, Y.; Sohl-Dickstein, J.; Kingma, D. P.; Kumar, A.; Ermon, S.; and Poole, B. 2021. Score-Based Generative Modeling through Stochastic Differential Equations. In *Proc. Int. Conf. Learn. Represent.*

Sunehag, P.; Lever, G.; Gruslys, A.; Czarnecki, W. M.; Zambaldi, V.; Jaderberg, M.; Lanctot, M.; Sonnerat, N.; Leibo, J. Z.; Tuyls, K.; and Graepel, T. 2018. Value-Decomposition Networks For Cooperative Multi-Agent Learning. In *Proc. Int. Conf. Auto. Agents Multiagent Syst.*, 2085–2087.

Sutton, R. S.; Precup, D.; and Singh, S. 1999. Between MDPs and semi-MDPs: A framework for temporal abstraction in reinforcement learning. *Artif. Intell.*, 112(1-2): 181–211.

Tian, Z.; Chen, R.; Hu, X.; Li, L.; Zhang, R.; Wu, F.; Peng, S.; Guo, J.; Du, Z.; Guo, Q.; and Chen, Y. 2023. Decompose a Task into Generalizable Subtasks in Multi-Agent Reinforcement Learning. In *Proc. Adv. Neural Inf. Process. Syst.*, volume 36, 78514–78532.

Venkatraman, S.; Khaitan, S.; Akella, R. T.; Dolan, J.; Schneider, J.; and Berseth, G. 2024. Reasoning with Latent Diffusion in Offline Reinforcement Learning. In *Proc. Int. Conf. Learn. Represent.*

Wang, J.; Ren, Z.; Liu, T.; Yu, Y.; and Zhang, C. 2021a. QPLEX: Duplex Dueling Multi-Agent Q-Learning. In *Proc. Int. Conf. Learn. Represent.*

Wang, T.; Dong, H.; Lesser, V.; and Zhang, C. 2020a. ROMA: Multi-Agent Reinforcement Learning with Emergent Roles. In *Proc. Int. Conf. Mach. Learn.*, volume 119, 9876–9886.

Wang, T.; Gupta, T.; Mahajan, A.; Peng, B.; Whiteson, S.; and Zhang, C. 2021b. RODE: Learning Roles to Decompose Multi-Agent Tasks. In *Proc. Int. Conf. Learn. Represent.*

Wang, T.; Wang, J.; Zheng, C.; and Zhang, C. 2020b. Learning Nearly Decomposable Value Functions via Communication Minimization. In *Proc. Int. Conf. Learn. Represent.*

Wang, W.; Yang, T.; Liu, Y.; Hao, J.; Hao, X.; Hu, Y.; Chen, Y.; Fan, C.; and Gao, Y. 2023. ASN: Action Semantics Network for Multiagent Reinforcement Learning. *Autonomous Agents and Multi-Agent Systems*, 37(1): 1–28.

Wang, Z.; Hunt, J. J.; and Zhou, M. 2023. Diffusion Policies as an Expressive Policy Class for Offline Reinforcement Learning. In *Proc. Int. Conf. Learn. Represent.*

Wen, M.; Kuba, J. G.; Lin, R.; Zhang, W.; Wen, Y.; Wang, J.; and Yang, Y. 2022. Multi-Agent Reinforcement Learning is a Sequence Modeling Problem. In *Proc. Adv. Neural Inf. Process. Syst.*, volume 35, 24602–24616.

Xu, Q.; Zhu, Y.; Wu, X.; and Chen, C. 2025. High-order Interactions Modeling for Interpretable Multi-Agent Q-Learning. In *Proc. Adv. Neural Inf. Process. Syst.*, volume 38.

Xu, Z.; Bai, Y.; Zhang, B.; Li, D.; and Fan, G. 2023. HAVEN: Hierarchical Cooperative Multi-Agent Reinforcement Learning with Dual Coordination Mechanism. In *Proc. AAAI Conf. Artif. Intell.*, volume 37, 11735–11743.

Yang, J.; Borovikov, I.; and Zha, H. 2020. Hierarchical Cooperative Multi-Agent Reinforcement Learning with Skill Discovery. In *Proc. Int. Conf. Auto. Agents Multiagent Syst.*, 1566–1574.

Yang, M.; Zhao, J.; Hu, X.; Zhou, W.; Zhu, J.; and Li, H. 2022a. LDSA: Learning Dynamic Subtask Assignment in Cooperative Multi-Agent Reinforcement Learning. In *Proc. Adv. Neural Inf. Process. Syst.*, volume 35, 11735–11743.

Yang, Y.; Chen, G.; Wang, W.; Hao, X.; Hao, J.; and Heng, P.-A. 2022b. Transformer-based Working Memory for Multiagent Reinforcement Learning with Action Parsing. In *Proc. Adv. Neural Inf. Process. Syst.*, volume 35, 1–14.

Zang, Y.; He, J.; Li, K.; Fu, H.; Fu, Q.; Xing, J.; and Cheng, J. 2023. Automatic Grouping for Efficient Cooperative Multi-Agent Reinforcement Learning. In *Proc. Adv. Neural Inf. Process. Syst.*, volume 36, 64896–64917.

Zhang, C.; and Lesser, V. 2011. Coordinated multi-agent reinforcement learning in networked distributed POMDPs. In *Proc. AAAI Conf. Artif. Intell.*, volume 25, 764–770.

Zhang, C.; Lesser, V. R.; and Abdallah, S. 2010. Self-Organization for Coordinating Decentralized Reinforcement Learning. In *Proc. Int. Conf. Auto. Agents Multiagent Syst.*, 739–746.

Zhang, K.; Sun, T.; Tao, Y.; Genc, S.; Mallya, S.; and Basar, T. 2020. Robust multi-agent reinforcement learning with model uncertainty. In *Proc. Adv. Neural Inf. Process. Syst.*, volume 33, 10571–10583.

Zhang, M.; Cai, Z.; Pan, L.; Hong, F.; Guo, X.; Yang, L.; and Liu, Z. 2024. Motiondiffuse: Text-driven human motion generation with diffusion model. *IEEE Trans. Pattern Anal. Mach. Intell.*, 46(6): 4115–4128.

A. Diffusion Model for Latent Representation Learning

Forward Inference of Diffusion Models

The forward process involves systematically adding noise to the original data, which serves as a fundamental part in comprehending the underlying principles of the diffusion model and preparing training samples essential for model development. Given an original latent representation $\mathbf{z}_0 \sim q(x)$, the diffusion forward process adds Gaussian noise to it through times cumulatively to obtain $\mathbf{z}_1, \mathbf{z}_2, \dots, \mathbf{z}_K$, as shown in the following formula. Here, a series of hyperparameters of the Gaussian distribution variance $\{\beta_k \in (0, 1)\}_{k=1}^K$ needs to be given. Since each timestep k of the forward process is only related to the timestep $k - 1$, it can also be regarded as a Markov process:

$$q(\mathbf{z}_k | \mathbf{z}_{k-1}) = \mathcal{N}\left(\mathbf{z}_k; \sqrt{1 - \beta_k} \mathbf{z}_{k-1}, \beta_k I\right), q(\mathbf{z}_{1:K} | \mathbf{z}_0) = \prod_{k=1}^K q(\mathbf{z}_k | \mathbf{z}_{k-1}). \quad (10)$$

When $K \rightarrow \infty$, \mathbf{z}_K is a complete Gaussian noise, which is related to the choice of the mean coefficient $\sqrt{1 - \beta_k}$, and in practice β_k increases as t increases, that is $\beta_1 < \beta_2 < \dots < \beta_K$.

To enable gradient backpropagation through the entire process, the diffusion model adopts the reparameterization trick, commonly used in works such as (Jang, Gu, and Poole 2017; Kingma and Welling 2014). Directly sampling from a distribution, e.g., a Gaussian distribution, is non-differentiable. Since sampling \mathbf{z}_k with Gaussian noise is pervasive in diffusion, reparameterization is required to ensure differentiability. Specifically, sampling $\mathbf{z} \sim \mathcal{N}(\mu_\theta, \sigma_\theta^2 I)$ can be reformulated as

$$\mathbf{z} = \mu_\theta + \sigma_\theta \odot \epsilon, \epsilon \in \mathcal{N}(0, I), \quad (11)$$

where ϵ is an independent random variable guiding the randomness, making the process differentiable. \mathbf{z} still satisfies the Gaussian distribution with mean μ_θ and variance σ_θ^2 . Here, μ_θ and σ_θ^2 can be inferred from a neural network with parameter θ . The entire sampling process is still gradient-differentiable, and the randomness is transferred to ϵ .

Obtaining \mathbf{z}_k through \mathbf{z}_0 and β is significant in the subsequent inference and deduction of the diffusion model. At first, we assume $\alpha_k = 1 - \beta_k$, and $\bar{\alpha}_k = \prod_{i=1}^k \alpha_i$. By expanding \mathbf{z}_k , we can then obtain

$$\begin{aligned} \mathbf{z}_k &= \sqrt{\alpha_k} \mathbf{z}_{k-1} + \sqrt{1 - \alpha_k} \epsilon_1 \quad \text{where } \epsilon_1, \epsilon_2, \dots \sim \mathcal{N}(0, \mathbf{I}); \\ &= \sqrt{\alpha_k} \left(\sqrt{\alpha_{k-1}} \mathbf{z}_{k-2} + \sqrt{1 - \alpha_{k-1}} \epsilon_2 \right) + \sqrt{1 - \alpha_k} \epsilon_1 \\ &= \sqrt{\alpha_k \alpha_{k-1}} \mathbf{z}_{k-2} + \left(\sqrt{\alpha_k(1 - \alpha_{k-1})} \epsilon_2 + \sqrt{1 - \alpha_k} \epsilon_1 \right) \\ &= \sqrt{\alpha_k \alpha_{k-1}} \mathbf{z}_{k-2} + \sqrt{1 - \alpha_k \alpha_{k-1}} \bar{\epsilon}_2 \quad \text{where } \bar{\epsilon}_2 \sim \mathcal{N}(0, \mathbf{I}); \\ &= \dots \\ &= \sqrt{\bar{\alpha}_k} \mathbf{z}_0 + \sqrt{1 - \bar{\alpha}_k} \bar{\mathbf{z}}_k. \end{aligned} \quad (12)$$

Since independent Gaussian distributions are additive, that is $\mathcal{N}(0, \sigma_1^2 I) + \mathcal{N}(0, \sigma_2^2 I) \sim \mathcal{N}(0, (\sigma_1^2 I + \sigma_2^2))$, we have

$$\sqrt{\alpha_k(1 - \alpha_{k-1})} \mathbf{z}_2 + \sqrt{1 - \alpha_k} \mathbf{z}_1 \sim \mathcal{N}(0, [\alpha_k(1 - \alpha_{k-1}) + (1 - \alpha_k)] I) = \mathcal{N}(0, (1 - \alpha_k \alpha_{k-1}) I). \quad (13)$$

Therefore, we can mix two Gaussian distributions to obtain a mixed Gaussian distribution with a standard deviation of $\sqrt{1 - \alpha_k \alpha_{k-1}}$, and $\bar{\epsilon}_2$ in Eq. (12) is still a standard Gaussian distribution. Under the circumstance, \mathbf{z}_k satisfies

$$q(\mathbf{z}_k | \mathbf{z}_0) = \mathcal{N}\left(\mathbf{z}_k; \sqrt{\bar{\alpha}_k} \mathbf{z}_0, (1 - \bar{\alpha}_k) I\right). \quad (14)$$

Reverse Inference of Diffusion Process

To reconstruct the true sample from Gaussian noise, where $\mathbf{z}_K \sim \mathcal{N}(\mathbf{0}, \mathbf{I})$, one can reverse the forward process and sample from the conditional distribution $q(\mathbf{z}_{k-1} | \mathbf{z}_k)$. It is worth noting that if β_k is sufficiently small, $q(\mathbf{z}_{k-1} | \mathbf{z}_k)$ will also follow a Gaussian distribution. However, directly estimating $q(\mathbf{z}_{k-1} | \mathbf{z}_k)$ is computationally intractable, as it requires access to the entire dataset. To address this, we learn a model p_θ to approximate these conditional probabilities, enabling the reverse diffusion process:

$$p_\theta(\mathbf{z}_{0:K}) = p(\mathbf{z}_K) \prod_{k=1}^K p_\theta(\mathbf{z}_{k-1} | \mathbf{z}_k), \quad p_\theta(\mathbf{z}_{k-1} | \mathbf{z}_k) = \mathcal{N}(\mathbf{z}_{k-1}; \mu_\theta(\mathbf{z}_k, k), \Sigma_\theta(\mathbf{z}_k, k)), \quad (15)$$

where $\mu_\theta(\mathbf{z}_k, k)$ and $\Sigma_\theta(\mathbf{z}_k, k)$ are parameterized by the learned model.

It is noteworthy that the reverse conditional probability becomes tractable when conditioned on \mathbf{z}_0 :

$$q(\mathbf{z}_{k-1} | \mathbf{z}_k, \mathbf{z}_0) = \mathcal{N}(\mathbf{z}_{k-1}; \tilde{\mu}(\mathbf{z}_k, \mathbf{z}_0), \tilde{\beta}_k \mathbf{I}).$$

Using the rule of Bayes, the conditional probability can be expressed as

$$\begin{aligned}
q(\mathbf{z}_{k-1} | \mathbf{z}_k, \mathbf{z}_0) &= q(\mathbf{z}_k | \mathbf{z}_{k-1}, \mathbf{z}_0) \frac{q(\mathbf{z}_{k-1} | \mathbf{z}_0)}{q(\mathbf{z}_k | \mathbf{z}_0)} \\
&\propto \exp \left(-\frac{1}{2} \left(\frac{(\mathbf{z}_k - \sqrt{\alpha_k} \mathbf{z}_{k-1})^2}{\beta_k} + \frac{(\mathbf{z}_{k-1} - \sqrt{\bar{\alpha}_{k-1}} \mathbf{z}_0)^2}{1 - \bar{\alpha}_{k-1}} - \frac{(\mathbf{z}_k - \sqrt{\bar{\alpha}_k} \mathbf{z}_0)^2}{1 - \bar{\alpha}_k} \right) \right) \\
&= \exp \left(-\frac{1}{2} \left(\left(\frac{\alpha_k}{\beta_k} + \frac{1}{1 - \bar{\alpha}_{k-1}} \right) \mathbf{z}_{k-1}^2 - \left(\frac{2\sqrt{\alpha_k}}{\beta_k} \mathbf{z}_k + \frac{2\sqrt{\bar{\alpha}_{k-1}}}{1 - \bar{\alpha}_{k-1}} \mathbf{z}_0 \right) \mathbf{z}_{k-1} + C(\mathbf{z}_k, \mathbf{z}_0) \right) \right),
\end{aligned}$$

where $C(\mathbf{z}_k, \mathbf{z}_0)$ is a term independent of \mathbf{z}_{k-1} and is omitted here.

Following the standard Gaussian density function, the mean and variance can be parameterized as follows, given the assumption that $\alpha_k = 1 - \beta_k$ and $\bar{\alpha}_k = \prod_{i=1}^k \alpha_i$ in Eq. (12):

$$\begin{aligned}
\tilde{\mu}_k(\mathbf{z}_k, \mathbf{z}_0) &= \left(\frac{\sqrt{\alpha_k}}{\beta_k} \mathbf{z}_k + \frac{\sqrt{\bar{\alpha}_{k-1}}}{1 - \bar{\alpha}_{k-1}} \mathbf{z}_0 \right) / \left(\frac{\alpha_k}{\beta_k} + \frac{1}{1 - \bar{\alpha}_{k-1}} \right) \\
&= \left(\frac{\sqrt{\alpha_k}}{\beta_k} \mathbf{z}_k + \frac{\sqrt{\bar{\alpha}_{k-1}}}{1 - \bar{\alpha}_{k-1}} \mathbf{z}_0 \right) \cdot \frac{1 - \bar{\alpha}_{k-1}}{1 - \bar{\alpha}_k} \cdot \beta_k \\
&= \frac{\sqrt{\alpha_k}(1 - \bar{\alpha}_{k-1})}{1 - \bar{\alpha}_k} \mathbf{z}_k + \frac{\sqrt{\bar{\alpha}_{k-1}}\beta_k}{1 - \bar{\alpha}_k} \mathbf{z}_0,
\end{aligned} \tag{16}$$

$$\begin{aligned}
\tilde{\beta}_k &= 1 / \left(\frac{\alpha_k}{\beta_k} + \frac{1}{1 - \bar{\alpha}_{k-1}} \right) \\
&= 1 / \left(\frac{\alpha_k - \bar{\alpha}_{k-1} + \beta_k}{\beta_k(1 - \bar{\alpha}_{k-1})} \right) \\
&= \frac{1 - \bar{\alpha}_{k-1}}{1 - \bar{\alpha}_k} \cdot \beta_k.
\end{aligned}$$

Combining the property of Eq. (14), we can represent $\mathbf{z}_0 = \frac{1}{\sqrt{\bar{\alpha}_k}} (\mathbf{z}_k - \sqrt{1 - \bar{\alpha}_k} \boldsymbol{\epsilon}_k)$ and plug it into Eq. (16):

$$\begin{aligned}
\tilde{\mu}_k &= \frac{\sqrt{\alpha_k}(1 - \bar{\alpha}_{k-1})}{1 - \bar{\alpha}_k} \mathbf{z}_k + \frac{\sqrt{\bar{\alpha}_{k-1}}\beta_k}{1 - \bar{\alpha}_k} \cdot \frac{1}{\sqrt{\bar{\alpha}_k}} (\mathbf{z}_k - \sqrt{1 - \bar{\alpha}_k} \boldsymbol{\epsilon}_k) \\
&= \frac{1}{\sqrt{\bar{\alpha}_k}} \left(\mathbf{z}_k - \frac{1 - \alpha_k}{\sqrt{1 - \bar{\alpha}_k}} \boldsymbol{\epsilon}_k \right).
\end{aligned} \tag{17}$$

Based on Eq. (14) and Eq. (15), the proposed setup is closely aligned with the Variational Auto-encoder (VAE) (Kingma and Welling 2014) framework, allowing us to employ the variational lower bound (VLB) to optimize the negative log-likelihood:

$$\begin{aligned}
-\log p_{\theta}(\mathbf{z}_0) &\leq -\log p(\mathbf{z}_0) + D_{\text{KL}}(q(\mathbf{z}_{1:K} | \mathbf{z}_0) \| p_{\theta}(\mathbf{z}_{1:K} | \mathbf{z}_0)) \\
&= -\log p(\mathbf{z}_0) + \mathbb{E}_{\mathbf{z}_{1:K} \sim q(\mathbf{z}_{1:K} | \mathbf{z}_0)} \left[\log \frac{q(\mathbf{z}_{1:K} | \mathbf{z}_0)}{p_{\theta}(\mathbf{z}_{1:K} | \mathbf{z}_0) / p_{\theta}(\mathbf{z}_0)} \right] \\
&= -\log p(\mathbf{z}_0) + \mathbb{E}_q \left[\log \frac{q(\mathbf{z}_{1:K} | \mathbf{z}_0)}{p_{\theta}(\mathbf{z}_{1:K} | \mathbf{z}_0)} \right] + \log p_{\theta}(\mathbf{z}_0) \\
&= \mathbb{E}_q \left[\log \frac{q(\mathbf{z}_{1:K} | \mathbf{z}_0)}{p_{\theta}(\mathbf{z}_0 : \mathbf{z}_K)} \right].
\end{aligned}$$

$$\text{Let } \mathcal{L}_{\text{VLB}} = \mathbb{E}_{q(\mathbf{z}_{0:K})} \left[\log \frac{q(\mathbf{z}_{1:K} | \mathbf{z}_0)}{p_{\theta}(\mathbf{z}_{1:K} | \mathbf{z}_0)} \right] \geq -\mathbb{E}_{q(\mathbf{z}_0)} \log p_{\theta}(\mathbf{z}_0).$$

We can also derive the same result by applying Jensen's inequality. Suppose our goal is to minimize the cross-entropy as the

learning objective:

$$\begin{aligned}
\mathcal{L}_{CE} &= -\mathbb{E}_{q(\mathbf{z}_0)} \log p_{\theta}(\mathbf{z}_0) \\
&= -\mathbb{E}_{q(\mathbf{z}_0)} \log \left(\int p_{\theta}(\mathbf{z}_{0:K}) d\mathbf{z}_{1:K} \right) \\
&= -\mathbb{E}_{q(\mathbf{z}_0)} \log \left(\int q(\mathbf{z}_{1:K}|\mathbf{z}_0) \frac{p_{\theta}(\mathbf{z}_{0:K})}{q(\mathbf{z}_{1:K}|\mathbf{z}_0)} d\mathbf{z}_{1:K} \right) \\
&= -\mathbb{E}_{q(\mathbf{z}_0)} \log \left(\mathbb{E}_{q(\mathbf{z}_{1:K}|\mathbf{z}_0)} \left[\frac{p_{\theta}(\mathbf{z}_{0:K})}{q(\mathbf{z}_{1:K}|\mathbf{z}_0)} \right] \right) \\
&\leq -\mathbb{E}_{q(\mathbf{z}_{0:K})} \log \left(\frac{p_{\theta}(\mathbf{z}_{0:K})}{q(\mathbf{z}_{1:K}|\mathbf{z}_0)} \right) \\
&= \mathbb{E}_{q(\mathbf{z}_{0:K})} \left[\log \frac{q(\mathbf{z}_{1:K}|\mathbf{z}_0)}{p_{\theta}(\mathbf{z}_{0:K})} \right] = \mathcal{L}_{VLB}.
\end{aligned}$$

To convert each term in the equation to be analytically computable, the objective can be further rewritten to be a combination of several KL-divergence and entropy terms (Sohl-Dickstein et al. 2015b):

$$\begin{aligned}
\mathcal{L}_{VLB} &= \mathbb{E}_{q(\mathbf{z}_{0:K})} \left[\log \frac{q(\mathbf{z}_{1:K}|\mathbf{z}_0)}{p_{\theta}(\mathbf{z}_{0:K})} \right] \\
&= \mathbb{E}_q \left[\log \frac{\prod_{k=1}^K q(\mathbf{z}_k|\mathbf{z}_{k-1})}{p_{\theta}(\mathbf{z}_K) \prod_{k=1}^K p_{\theta}(\mathbf{z}_{k-1}|\mathbf{z}_k)} \right] \\
&= \mathbb{E}_q \left[-\log p_{\theta}(\mathbf{z}_K) + \sum_{k=1}^K \log \frac{q(\mathbf{z}_k|\mathbf{z}_{k-1})}{p_{\theta}(\mathbf{z}_{k-1}|\mathbf{z}_k)} \right] \\
&= \mathbb{E}_q \left[-\log p_{\theta}(\mathbf{z}_K) + \sum_{k=2}^K \log \frac{q(\mathbf{z}_k|\mathbf{z}_{k-1})}{p_{\theta}(\mathbf{z}_{k-1}|\mathbf{z}_k)} + \log \frac{q(\mathbf{z}_1|\mathbf{z}_0)}{p_{\theta}(\mathbf{z}_0|\mathbf{z}_1)} \right] \\
&= \mathbb{E}_q \left[-\log p_{\theta}(\mathbf{z}_K) + \sum_{k=2}^K \log \frac{q(\mathbf{z}_k|\mathbf{z}_{k-1}, \mathbf{z}_0)}{p_{\theta}(\mathbf{z}_{k-1}|\mathbf{z}_k)} + \log \frac{q(\mathbf{z}_K|\mathbf{z}_0)}{p_{\theta}(\mathbf{z}_K)} \right] \\
&= \mathbb{E}_q \left[\log \frac{q(\mathbf{z}_K|\mathbf{z}_0)}{p_{\theta}(\mathbf{z}_K)} + \sum_{k=2}^K \log \frac{q(\mathbf{z}_k|\mathbf{z}_{k-1}, \mathbf{z}_0)}{p_{\theta}(\mathbf{z}_{k-1}|\mathbf{z}_k)} - \log p_{\theta}(\mathbf{z}_0|\mathbf{z}_1) \right] \\
&= \mathbb{E}_q \left[\underbrace{D_{\text{KL}}(q(\mathbf{z}_K|\mathbf{z}_0) \| p_{\theta}(\mathbf{z}_K))}_{\mathcal{L}_K} + \sum_{k=2}^K \underbrace{D_{\text{KL}}(q(\mathbf{z}_{k-1}|\mathbf{z}_k, \mathbf{z}_0) \| p_{\theta}(\mathbf{z}_{k-1}|\mathbf{z}_k))}_{\mathcal{L}_{k-1}} - \underbrace{\log p_{\theta}(\mathbf{z}_0|\mathbf{z}_1)}_{\mathcal{L}_0} \right]. \quad (18)
\end{aligned}$$

The variational lower bound can be expressed using the labels from Eq. (18) as follows:

$$\mathcal{L}_{VLB} = \mathcal{L}_K + \sum_{k=1}^{K-1} \mathcal{L}_k + \mathcal{L}_0.$$

Every KL term in \mathcal{L}_{VLB} (except for \mathcal{L}_0) compares two Gaussian distributions, and therefore they can be computed in a closed form. \mathcal{L}_K is constant and can be ignored during training because q has no learnable parameters, and \mathbf{z}_K is Gaussian noise. Previous method (Ho, Jain, and Abbeel 2020) models \mathcal{L}_0 using a separate discrete decoder derived from $\mathcal{N}(\mathbf{z}_0; \mu_{\theta}(\mathbf{z}_1, 1), \Sigma_{\theta}(\mathbf{z}_1, 1))$.

Parameterization of L_k for Training Loss

In order to train a neural network to approximate the conditional probability distributions from Eq. (15) in the reverse diffusion process:

$$p_{\theta}(\mathbf{z}_{k-1}|\mathbf{z}_k) = \mathcal{N}(\mathbf{z}_{k-1}; \mu_{\theta}(\mathbf{z}_k, k), \Sigma_{\theta}(\mathbf{z}_k, k)),$$

we adopt the approach of training μ_θ to predict $\tilde{\mu}_k = \frac{1}{\sqrt{\alpha_k}} \left(\mathbf{z}_k - \frac{1-\alpha_k}{\sqrt{1-\bar{\alpha}_k}} \boldsymbol{\epsilon}_k \right)$. Given that \mathbf{z}_k is accessible as input during training, we can reparameterize the Gaussian noise term to directly predict $\boldsymbol{\epsilon}_k$ from the input \mathbf{z}_k at timestep k :

$$\begin{aligned} \mu_\theta(\mathbf{z}_k, k) &= \frac{1}{\sqrt{\alpha_k}} \left(\mathbf{z}_k - \frac{1-\alpha_k}{\sqrt{1-\bar{\alpha}_k}} \boldsymbol{\epsilon}_\theta(\mathbf{z}_k, k) \right), \\ \text{thus } \mathbf{z}_{k-1} &= \mathcal{N} \left(\mathbf{z}_{k-1}; \frac{1}{\sqrt{\alpha_k}} \left(\mathbf{z}_k - \frac{1-\alpha_k}{\sqrt{1-\bar{\alpha}_k}} \boldsymbol{\epsilon}_\theta(\mathbf{z}_k, k) \right), \Sigma_\theta(\mathbf{z}_k, k) \right). \end{aligned}$$

The loss term \mathcal{L}_k is parameterized to minimize the difference from $\tilde{\mu}$:

$$\begin{aligned} \mathcal{L}_k &= \mathbb{E}_{\mathbf{z}_0, \boldsymbol{\epsilon}} \left[\frac{1}{2\|\Sigma_\theta(\mathbf{z}_k, k)\|_2^2} \|\tilde{\mu}_k(\mathbf{z}_k, \mathbf{z}_0) - \mu_\theta(\mathbf{z}_k, k)\|^2 \right] \\ &= \mathbb{E}_{\mathbf{z}_0, \boldsymbol{\epsilon}} \left[\frac{1}{2\|\Sigma_\theta\|_2^2} \left\| \frac{1}{\sqrt{\alpha_k}} \left(\mathbf{z}_k - \frac{1-\alpha_k}{\sqrt{1-\bar{\alpha}_k}} \boldsymbol{\epsilon} \right) - \frac{1}{\sqrt{\alpha_k}} \left(\mathbf{z}_k - \frac{1-\alpha_k}{\sqrt{1-\bar{\alpha}_k}} \boldsymbol{\epsilon}_\theta(\mathbf{z}_k, k) \right) \right\|^2 \right] \\ &= \mathbb{E}_{\mathbf{z}_0, \boldsymbol{\epsilon}} \left[\frac{(1-\alpha_k)^2}{2\alpha_k(1-\bar{\alpha}_k)\|\Sigma_\theta\|_2^2} \|\boldsymbol{\epsilon} - \boldsymbol{\epsilon}_\theta(\mathbf{z}_k, k)\|^2 \right] \\ &= \mathbb{E}_{\mathbf{z}_0, \boldsymbol{\epsilon}} \left[\frac{(1-\alpha_k)^2}{2\alpha_k(1-\bar{\alpha}_k)\|\Sigma_\theta\|_2^2} \|\boldsymbol{\epsilon} - \boldsymbol{\epsilon}_\theta(\sqrt{\bar{\alpha}_k}\mathbf{z}_0 + \sqrt{1-\bar{\alpha}_k}\boldsymbol{\epsilon}, k)\|^2 \right]. \end{aligned} \quad (19)$$

Empirically, the training procedure works better with a simplified objective from Eq. (19) that ignores the weighting term:

$$\begin{aligned} \mathcal{L}_d(\theta) &= \mathbb{E}_{k \sim [1, K], \mathbf{z}_0, \boldsymbol{\epsilon}_k} \left[\|\boldsymbol{\epsilon}_k - \boldsymbol{\epsilon}_\theta(\mathbf{z}_k, k)\|^2 \right] \\ &= \mathbb{E}_{k \sim [1, K], \mathbf{z}_0, \boldsymbol{\epsilon}_k} \left[\|\boldsymbol{\epsilon}_k - \boldsymbol{\epsilon}_\theta(\sqrt{\bar{\alpha}_k}\mathbf{z}_0 + \sqrt{1-\bar{\alpha}_k}\boldsymbol{\epsilon}_k, k)\|^2 \right] \\ &= \mathbb{E}_{k \sim [1, K], \mathbf{z}_0, \boldsymbol{\epsilon}_k} \left[\|\boldsymbol{\epsilon}_k - \boldsymbol{\epsilon}_\theta(\sqrt{\bar{\alpha}_k}\mathbf{z}_0 + \sqrt{1-\bar{\alpha}_k}\boldsymbol{\epsilon}_k, k)\|^2 \right]. \end{aligned}$$

B. Theoretical Analysis of Subtask-based Value Decomposition

In this section, we theoretically derive the expansion formula for each individual Q-value function and further explore the non-linear combination of multiple individual Q-values into a global Q-value under the multi-agent value decomposition framework.

Following the general framework of MARL, the Q-value $Q_{tot}(s, \mathbf{a})$ is a function on the state vector s and joint actions $\mathbf{a} = (a_1, \dots, a_N)$. By applying the implicit function theorem, Q_{tot} can also be viewed as a function in terms of individual Q-value Q_i :

$$Q_{tot} = Q_{tot}(s, Q_1, Q_2, \dots, Q_N), \text{ where } Q_i = Q_i(s, a_i) \approx Q_i(\tau_i, a_i).$$

To simplify our analysis, we assume that no agent operates independently of the group. In this context, an agent i either contributes to the group or is treated as an individual optimizing its own policy. Mathematically, this ensures that $\frac{\partial Q_{tot}}{\partial Q_i}$ is not identically zero, meaning that variations in Q_i generally influence Q_{tot} , though it may vanish at certain points:

$$\frac{\partial Q_{tot}}{\partial Q_i} \neq 0.$$

We investigate the local behaviors of Q_{tot} and Q_i nearly a maximum point \mathbf{a} in the action space assuming the state s is fixed. Since the gradient $\frac{\partial Q_{tot}}{\partial \mathbf{a}}$ vanishes at the optimum point \mathbf{a}_o , we have

$$\frac{\partial Q_{tot}}{\partial a_i} = \frac{\partial Q_{tot}}{\partial Q_i} \frac{\partial Q_i}{\partial a_i} = 0.$$

We conclude that

$$\frac{\partial Q_i}{\partial a_i}(a^o) = 0.$$

Consequently, we have local expansion of $Q_i(a_i)$ as follows:

$$Q_i(a_i) = \alpha_i + \beta_i(a_i - a_i^o)^2 + o((a_i - a_i^o)^2), \quad (20)$$

where α_i and β_i are constants. Thereafter, we can theoretically derive that the non-linear dependence of the global Q-value Q_{tot} on individual Q-value Q_i (near a maximal point \mathbf{a}^o) as shown in the following Theorem 1.

Theorem 1. Assume that the action space is continuous and there is no independent agent. Then there exist constants $c(s)$, $\lambda_{i,h}(s)$ (depending on state s), such that the local expansion of Q_{tot} admits the following form:

$$Q_{tot}(s, \mathbf{a}) \approx c(s) + \sum_{i,h} \lambda_{i,h}(s) Q_i(\tau_i, a_i). \quad (21)$$

where $\lambda_{i,h}$ is a linear functional of all partial derivatives $\frac{\partial^h Q_{tot}}{\partial Q_{i_1} \dots \partial Q_{i_h}}$ of order h , and decays super-exponentially fast in h .

Proof. We expand Q_{tot} in terms of Q_i :

$$Q_{tot} = c + \sum_i \mu_i Q_i + \sum_{i,j} \mu_{ij} Q_i Q_j + \dots + \sum_{i_1, \dots, i_k} \mu_{i_1, \dots, i_k} Q_{i_1} \dots Q_{i_k} + \dots \quad (22)$$

where

$$\mu_i = \frac{\partial Q_{tot}}{\partial Q_i}, \quad \mu_{ij} = \frac{1}{2} \frac{\partial^2 Q_{tot}}{\partial Q_i \partial Q_j},$$

and in general

$$\mu_{i_1, \dots, i_k} = \frac{1}{k!} \frac{\partial^k Q_{tot}}{\partial Q_{i_1} \dots \partial Q_{i_k}}.$$

Recall Eq. (20) for each individual Q value, we have a local expansion

$$Q_i(a_i) = \alpha_i + \beta_i(a_i - a_i^o)^2 + o((a_i - a_i^o)^2).$$

Now we apply the above equation to the second-order term in Eq. (21):

$$\begin{aligned} \sum_{i,j} \mu_{ij} Q_i Q_j &= \sum_{i,j} \mu_{ij} (\alpha_i + \beta_i(a_i - a_i^o)^2) (\alpha_j + \beta_j(a_j - a_j^o)^2) + o(\|a - a^o\|^2) \\ &= \sum_{i,j} \mu_{ij} \alpha_i \alpha_j + 2 \sum_{i,j} \mu_{ij} \alpha_i \beta_j (a_j - a_j^o)^2 + o(\|a - a^o\|^2) \\ &= \sum_{i,j} \mu_{ij} \alpha_i \alpha_j + 2 \sum_{i,j} \mu_{ij} \alpha_j (Q_i - \alpha_i) + o(\|a - a^o\|^2) \\ &= - \sum_{i,j} \mu_{ij} \alpha_i \alpha_j + 2 \sum_{i,j} \mu_{ij} \alpha_j Q_i + o(\|a - a^o\|^2). \end{aligned}$$

Therefore, we will take

$$\lambda_{i,2} = 2 \sum_j \mu_{ij} \alpha_j.$$

In general, we have

$$\mu_{i_1, \dots, i_k} = \frac{1}{k!} \frac{\partial^k Q_{tot}}{\partial Q_{i_1} \dots \partial Q_{i_k}},$$

and

$$\sum_{i_1, \dots, i_k} \mu_{i_1, \dots, i_k} Q_{i_1} \dots Q_{i_k} = (k-1) \sum_{i_1, \dots, i_k} \mu_{i_1, \dots, i_k} \alpha_{i_1} \dots \alpha_{i_{k-1}}.$$

Hence, we take

$$\lambda_{i,k} = k \sum_{i_1, \dots, i_k} \mu_{i_1, \dots, i_k} \alpha_{i_1} \dots \alpha_{i_{k-1}}.$$

The convergence of the series $\sum_k \lambda_{i,k}$ only requires mild conditions, for example, boundedness or even small growth of partial derivatives $\frac{\partial^k Q_{tot}}{\partial Q^1 \dots \partial Q^k}$ in terms of k . Hence, Theorem 1 is proved.

We use multiple attention heads to implement the approximations of different orders of partial derivatives. By summing up the head Q-values Q_h from different heads, we obtain

$$Q_{tot} \approx c(s) + \sum_{h=1}^H Q_h, \quad \text{where } Q_h = \sum_{i=1}^N \lambda_{i,h} Q_i, \quad (23)$$

H is the number of attention heads. Lastly, the first term $c(s)$ in Eq. (21) could be learned by a neural network with the global state s as the input. Our method naturally holds the monotonicity and then achieves the IGM property between Q_{tot} and Q_i :

$$\frac{\partial Q_{tot}}{\partial Q_i} \geq 0, \forall i \in \{1, 2, \dots, N\}.$$

Thus, CD³T allows tractable maximization of the joint action-value in off-policy learning and guarantees consistency between the centralized and decentralized policies.

C. Pseudo Code

Algorithm 1: CD³T in MARL

Input: B : The Boolean variable whether to update the action representation
 J : Number of clusters
 ΔT : Time interval for updating subtask selector
 N : Number of agents
 \mathcal{D} : Replay buffer
 T : Timesteps of a learning episode
 T_{tot} : Total timesteps of learning

- 1: Initialize all network parameters
- 2: Initialize the replay buffer \mathcal{D} for storing agent trajectories
- 3: **for** episode = 1, 2, ... **do**
- 4: Initialize history agent embedding h_i^0 and action vector a_i^0 for each agent
- 5: **for** $t = 1, 2, \dots, T$ **do**
- 6: Obtain each agent's partial observation $\{o_i^t\}_{i=1}^N$ and global state s_t
- 7: **if** $B = \text{True}$ **then**
- 8: **if** $T_{tot} < 50K$ **then**
- 9: **for** agent $i = 1, 2, \dots, N$ **do**
- 10: Calculate the action representation $z_{a_i}^t$
- 11: Update diffusion model according to Eq. (3)
- 12: **end for**
- 13: **else**
- 14: Partition action representations $\{z_{a_i}^t\}_{i=1}^N$ into J clusters $\{\phi^j\}_{j=1}^J$ using k -means
- 15: Calculate the subtask representation $z_{\phi^j}^t$
- 16: $B = \text{False}$
- 17: **end if**
- 18: **end if**
- 19: Execute joint action $a^t = [a_1^t, a_2^t, \dots, a_n^t]^\top$ and obtain global reward r^t
- 20: **end for**
- 21: Store the trajectory to \mathcal{D}
- 22: Sample a batch of trajectories from \mathcal{D}
- 23: **if** $T_{tot} \bmod \Delta T == 0$ **then**
- 24: Select subtask ϕ_j for each agent
- 25: Update the parameters of subtask selector Q-network and the mixing network according to Eq.(5)
- 26: **end if**
- 27: Update the parameters of the individual Q-network and the mixing network according to Eq.(8)
- 28: **end for**

D. Experimental Details

Benchmark and settings

In our paper, we introduce three types of testing benchmarks as shown in Fig. 9, including Level Based Foraging (LBF), StarCraft Multi-Agent Challenge (SMAC), and SMACv2. In this section, we describe the details and settings of these benchmarks.

StarCraft Multi-Agent Challenge. The StarCraft Multi-Agent Challenge (SMAC) (Samvelyan et al. 2019) is a seminal benchmark for assessing the efficacy of multi-agent reinforcement learning (MARL) algorithms in challenging cooperative and competitive environments. SMAC focuses on micromanagement scenarios in StarCraft II (SC 2.4.10 version), where allied units are exclusively controlled by reinforcement learning agents, and enemy units are governed by a built-in AI with a fixed difficulty level of difficulty=7. Agents must collaboratively devise sophisticated strategies to outmaneuver and defeat the adversaries within a predefined exploration horizon. In this study, we evaluate algorithmic performance across 8 highly challenging combat scenarios, ensuring consistency and reproducibility through standardized training steps. Table 1 presents a brief introduction of these scenarios and the maximum training step, and all experimental configurations strictly adhere to the original setup, as detailed in *Table 4*.

StarCraft Multi-Agent Challenge v2. The StarCraft Multi-Agent Challenge v2 (SMACv2) (Ellis et al. 2023) represents a significant evolution of the SMAC benchmark, designed to push the boundaries of MARL research by introducing heightened complexity and uncertainty. SMACv2 incorporates randomized initial configurations of enemy units, including their positions, attributes, and quantities, thus necessitating robust generalization capabilities. Furthermore, dynamic environmental features,



Figure 9: Three benchmarks used in our experiments.

such as map alterations and fluctuating objectives, create an additional layer of unpredictability. To ensure rigorous evaluation, we adopt uniform training step limits and leverage the SC2.4.10 environment version. In this work, we benchmark algorithms on 3 highly complex scenarios, with specific configurations outlined in *Table 2*, to comprehensively evaluate their adaptability and scalability.

Level Based Foraging. Level-Based Foraging (LBF) (Christanos, Schäfer, and Albrecht 2020) is a well-established benchmark that encapsulates the interplay of cooperative and competitive dynamics in multi-agent systems. Agents are deployed on a 10×10 grid, each endowed with a specific level, and their observations are confined to a local 5×5 region surrounding them. The primary objective is to collaboratively consume food items scattered across the grid, contingent upon the collective level of participating agents meeting or exceeding the food item’s level. Rewards are normalized based on the consumed food level, while a movement penalty of -0.002 incentivizes efficient exploration. This work considers two distinct task configurations: one comprising 4 agents and 2 food items, and another with 3 agents and 3 food items. Comprehensive experimental details are enumerated in *Table 3*.

Table 1: Introduction of scenarios in SMAC benchmark.

MAP NAME	ALLY UNITS	ENEMY UNITS	TOTAL Timesteps	SCENARIO TYPE
8m	8 MARINES	8 MARINES	1M	EASY
2s3z	2 STALKERS, 3 ZEALOTS	2 STALKERS, 3 ZEALOTS	1.5M	EASY
3s5z	3 STALKERS, 5 ZEALOTS	3 STALKERS, 5 ZEALOTS	1.5M	HARD
2c_vs_64zg	2 COLOSSI	64 ZERGLINGS	1.5M	HARD
5m_vs_6m	5 MARINES	6 MARINES	1.5M	HARD
3s5z_vs_3s6z	3 STALKERS, 5 ZEALOTS	3 STALKERS, 6 ZEALOTS	4M	SUPER HARD
corridor	6 ZEALOTS	24 ZERGLINGS	4M	SUPER HARD
6h_vs_8z	6 HYDRALISKS	8 ZEALOTS	4M	SUPER HARD

Table 2: Introduction of scenarios in SMACv2 benchmark.

MAP NAME	NUMBER OF ALLIES	NUMBER OF ENEMIES	UNIT COMPOSITION
Terran_10_vs_10	10	10	MARINES, MARAUDERS, MEDIVACS
Zerg_10_vs_10	10	10	ZERGLINGS, HYDRALISKS, BANELINGS
Protoss_10_vs_10	10	10	STALKERS, ZEALOTS, COLOSSI

Hyperparameters of Baselines

Our experiments are conducted using the PyMARL framework (Samvelyan et al. 2019), which we adopt to implement a range of baseline methods. These include five representative value-decomposition algorithms—VDN (Sunehag et al. 2018), QMIX (Rashid et al. 2018), QTRAN (Son et al. 2019), QPLEX (Wang et al. 2021a), and CDS (Li et al. 2021)—as well as four subtask-oriented approaches: RODE (Wang et al. 2021b), GoMARL (Zang et al. 2023), ACORM (Hu et al. 2024), and DT2GS (Tian et al. 2023). For fair comparison, all baselines are configured with consistent hyperparameters, following the default settings provided in the official PyMARL codebases and respective implementations. Our method is trained with

Table 3: Experimental Settings of Level-Based Foraging.

HYPERPARAMETER	VALUE	DESCRIPTION
MAX PLAYER LEVEL	3	MAXIMUM AGENT LEVEL ATTRIBUTE
MAX EPISODE LENGTH	50	MAXIMUM TIMESTEPS PER EPISODE
BATCH SIZE	32	NUMBER OF EPISODES PER UPDATE
TEST INTERVAL	10,000	FREQUENCY OF EVALUATING PERFORMANCE
TEST EPISODES	32	NUMBER OF EPISODES TO TEST
REPLAY BATCH SIZE	5000	MAXIMUM NUMBER OF EPISODES STORED IN MEMORY
DISCOUNT FACTOR γ	0.99	DEGREE OF IMPACT OF FUTURE REWARDS
TOTAL TIMESTEPS	1,050,000	NUMBER OF TRAINING STEPS
START ϵ	1.0	THE START ϵ VALUE TO EXPLORE
FINISH ϵ	0.05	THE FINISH ϵ VALUE TO EXPLORE
ANNEAL STEPS FOR ϵ	50,000	NUMBER OF STEPS OF LINEAR ANNEALING
TARGET UPDATE INTERVAL	200	THE TARGET NETWORK UPDATE CYCLE

Table 4: Experimental settings of SMAC and SMACv2.

HYPERPARAMETER	VALUE	DESCRIPTION
DIFFICULTY	7	ENEMY UNITS WITH BUILT-IN AI DIFFICULTY
BATCH SIZE (SMAC)	32	NUMBER OF EPISODES PER UPDATE
BATCH SIZE (SMACv2)	128	NUMBER OF EPISODES PER UPDATE
TEST INTERVAL	10,000	FREQUENCY OF EVALUATING PERFORMANCE
TEST EPISODES	32	NUMBER OF EPISODES TO TEST
REPLAY BATCH SIZE	5000	MAXIMUM NUMBER OF EPISODES IN MEMORY
DISCOUNT FACTOR γ	0.99	DEGREE OF IMPACT OF FUTURE REWARDS
START ϵ	1.0	THE START ϵ VALUE TO EXPLORE
FINISH ϵ	0.05	THE FINISH ϵ VALUE TO EXPLORE
ANNEAL STEPS FOR EASY & HARD	50,000	NUMBER OF STEPS OF LINEAR ANNEALING ϵ
ANNEAL STEPS FOR SUPER HARD	100,000	NUMBER OF STEPS OF LINEAR ANNEALING ϵ
TARGET UPDATE INTERVAL	200	THE TARGET NETWORK UPDATE CYCLE

evaluations every 20,000 environment steps, using 20 episodes and decentralized greedy action selection to estimate the test win rate. To ensure statistical robustness, we run all experiments with five random seeds in environments characterized by clear success/failure dynamics. The win rate is computed as the proportion of episodes in which the allied agents successfully eliminate all enemy units within the time limit. Optimization is performed using the RMSprop optimizer with a learning rate of 0.0005, and target network updates are conducted every 200 training episodes.

Hyperparameters of CD^3T

Our implementation of CD^3T is built upon the PyMARL framework. Agent observations are manually encoded and projected into a 32-dimensional hidden space. Each agent's policy network comprises an MLP layer followed by a GRU layer, with the final embedding dimension set to 64. All hyperparameters used in CD^3T are summarized in *Table 5*. Training is performed on a single machine equipped with an NVIDIA RTX 4090 GPU and an Intel Core i9-13900K CPU. The total training time varies depending on the complexity of the scenario.

Table 5: The special hyper-parameters of CD^3T architecture.

COMPONENT	HYPER-PARAMETERS	VALUE
DIFFUSION MODEL	START β	0.0001
	END β	0.02
	SCALING FACTOR λ_{dr}	10
	SCALING FACTOR η_e	0.1
SUBTASK SELECTOR	NUMBER OF SUBTASK CLUSTERS	3
	SUBTASK SELECTION INTERVAL	5
	STATE LATENT DIMENSION	32
	ACTION LATENT DIMENSION	20
	SUBTASK ACTION SPACES UPDATE START	50,000
MIXING NETWORK	STATE EMBEDDING DIMENSION	32
	NUMBER OF ATTENTION HEADS	8
	FIRST LAYER QUERY DIMENSION	64
	SECOND LAYER QUERY DIMENSION	32
	LAYER KEY DIMENSION	32
	FIRST LAYER WEIGHT DIMENSION	64
	SECOND LAYER WEIGHT DIMENSION	8

E. Performance on SMACv2

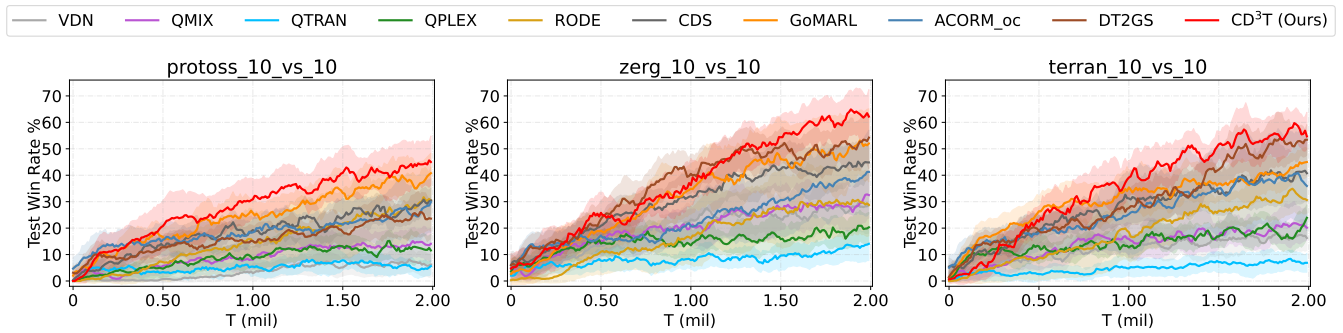


Figure 10: Performance comparison with baselines on SMACv2 scenarios.

The introduction of SMACv2 was motivated by the observation that many original SMAC maps lack sufficient diversity and stochasticity to effectively challenge state-of-the-art MARL algorithms. To evaluate the generalization and robustness of our proposed method under more complex and less predictable conditions, we benchmark CD^3T against several baselines on three redesigned scenarios in SMACv2: protoss_10_vs_10, zerg_10_vs_10, and terran_10_vs_10.

Figure 10 presents the comparative performance across these tasks. CD^3T achieves better results, suggesting enhanced adaptability in handling diverse and intricate coordination challenges. In contrast, traditional value factorization methods such as VDN, QMIX, QTRAN, and QPLEX exhibit notably weaker performance. This may reflect their limitations in modeling complex interactions, particularly due to rigid decomposition structures that often conflate individual utility with joint return signals. RODE performs less effectively, possibly due to its simplified semantic extraction mechanism and limited propagation of semantic context through the learning pipeline. The lack of fine-grained semantic representations may hinder accurate credit assignment under decentralized settings. CDS achieves reasonable performance, likely benefiting from its emphasis on promoting diversity among agents, which can be advantageous in dynamic environments with shifting coordination demands. GoMARL outperforms traditional baselines by leveraging group-level semantics to enrich the value decomposition process. ACORM also demonstrates relatively competitive results, indicating that its structure remains effective within the 2M timestep horizon, even without explicit clustering mechanisms. DT2GS shows performance close to that of CD^3T on `zerg_10_vs_10` and `terran_10_vs_10`, but underperforms on the more demanding `protoss_10_vs_10` task. This gap suggests that while DT2GS captures some useful subtask structure, its strong reliance on subtask transferability may limit its ability to adapt to task-specific complexities. Overall, these empirical results indicate that CD^3T is a promising method for dynamically decomposing and coordinating multi-agent tasks, which should be attributed to its use of conditional diffusion modeling and latent representation guidance in value factorization.

Table 6: Scalability comparison across QMIX, RODE, CD^3T and CD^3T (After 50K timesteps).

COMPONENT	QMIX	RODE	CD^3T	CD^3T (AFTER 50K TIMESTEPS)
AGENT NETWORK	27.5K	27.1K	27.1K	27.1K
MIXING NETWORK	18.8K	18.8K	23.2K	23.2K
DIFFUSION ENCODER	–	–	55.0K	–
OTHER MODULES	–	25.4K	22.9K	22.9K
TOTAL PARAMETERS	46.3K	71.3K	128.2K	73.2K

Model Scalability and Training Efficiency Analysis

To reduce memory overhead and improve training efficiency, we adopt a lightweight diffusion model, with detailed parameter statistics listed in Table 6. After the initial 50K timesteps, subtask assignments and their corresponding latent representations are fixed, eliminating the need to invoke the diffusion model for subsequent action representation generation. At this point, the overall parameter count of CD^3T becomes comparable to that of RODE. Since the first 50K timesteps constitute only a small portion of the total training horizon, the end-to-end training time of CD^3T remains similar to RODE—typically ranging from 1 to 4 million timesteps and requiring approximately 6 to 25 hours of wall-clock time, depending on scenario complexity. Despite operating under a comparable computational budget, CD^3T consistently outperforms all baselines across nearly all evaluated scenarios, highlighting its empirical effectiveness and scalability in diverse multi-agent tasks.

F. Related Work

Value-based MARL. Value-based MARL (Multi-Agent Reinforcement Learning) has witnessed significant advancements in recent years. A basic approach is Independent Q-Learning (IQL), which treats other agents as part of a non-stationary environment and trains separate Q-functions for each agent. Despite its simplicity, IQL often suffers from instability due to policy shifts among agents, leading to poor convergence. At the other extreme, centralized methods learn a joint Q-function over the full action-observation space, effectively capturing inter-agent dependencies. However, this comes at the cost of scalability, as the joint space grows exponentially with the number of agents.

To balance scalability and coordination, many recent methods adopt centralized training with decentralized execution (CTDE) via value function factorization. VDN (Sunehag et al. 2018) introduces a linear additive decomposition of the global Q-function. QMIX (Rashid et al. 2018) extends this with a monotonic mixing network, ensuring consistency between local and global values. QTRAN (Son et al. 2019) offers a more flexible formulation with theoretical guarantees, while QPLEX (Wang et al. 2021a) incorporates the Individual-Global-Max (IGM) principle into a duplex dueling architecture, enhancing expressiveness and learning efficiency. Improving credit assignment remains another key focus. CDS (Li et al. 2021) employs counterfactual baselines and agent-specific utilities to better align local contributions with global objectives. GoMARL (Zang et al. 2023) introduces group-wise factorization, partitioning agents into subsets to reduce the joint action space and improve scalability in large-scale scenarios. Beyond factorization, complementary advances span differentiable communication (Wang et al. 2020b), exploration strategies (Gupta et al. 2021), and robustness under non-stationarity (Zhang et al. 2020).

Building on these advancements, our method CD^3T introduces a hierarchical framework that leverages diffusion-based latent

representations for subtask discovery. These representations are fed into an attention-based mixing network to enable semantically guided and interpretable credit assignment, offering improved scalability and adaptability in complex MARL settings.

Hierarchical MARL. Hierarchical reinforcement learning (HRL) has been extensively studied in single-agent settings to address sparse rewards and facilitate transfer learning (Al-Emran 2015; Sutton, Precup, and Singh 1999). Existing works in HRL typically focus on decomposing tasks through either subgoal learning (Nair and Finn 2020; Dilokthanakul et al. 2019) or skill discovery (Daniel et al. 2016; Sharma et al. 2020).

Extending HRL to multi-agent scenarios introduces additional challenges, such as scalable communication and effective role differentiation (Wang et al. 2020a), which call for hierarchical coordination among agents (Zhang, Lesser, and Abdallah 2010). Early work, such as feudal RL (Dayan and Hinton 1992), adopts a manager-worker paradigm, where high-level managers assign goals and lower-level workers act to fulfill them. Bi-level hierarchies have also been successfully applied to discover agent-level skills (Lee, Yang, and Lim 2020; Yang, Borovikov, and Zha 2020). Recent efforts have extended hierarchical MARL to Markov games, where high-level policies govern strategic choices across agents (Wang et al. 2021b). In particular, HAVEN (Xu et al. 2023) introduces a hierarchical value decomposition framework with dual coordination mechanisms—across levels and across agents—enabling flexible cooperation without the need for domain-specific priors or pretraining. By combining structured credit assignment with hierarchical reasoning, HAVEN improves coordination in complex tasks.

Here, CD³T introduces a novel two-level hierarchical architecture that automatically identifies subtask structures and optimizes policies within each subspace. This design improves credit assignment, enhances sample efficiency, and enables robust performance in dynamic, high-dimensional multi-agent scenarios.

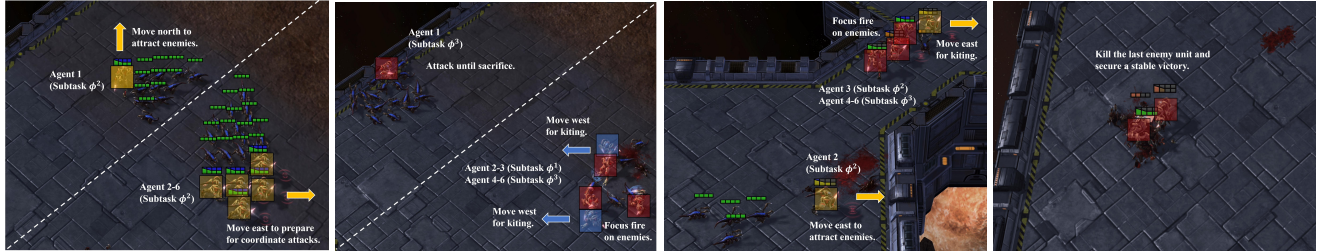
Diffusion Models for Reinforcement Learning. Diffusion models have recently emerged as a powerful class of generative frameworks, leveraging denoising processes to reverse multi-step noise corruptions and generate high-fidelity samples (Song et al. 2021). Their strong generative capacity has sparked growing interest in reinforcement learning (RL), leading to a range of innovative applications. A representative example is Diffuser (Janner et al. 2022), which learns a diffusion-based model from offline trajectories to perform goal-directed planning via guided sampling. Beyond trajectory generation, diffusion models have shown promise across multiple RL components, including serving as expressive policy parameterizations (Wang, Hunt, and Zhou 2023), enabling structured exploration through latent skill modeling (Venkatraman et al. 2024), and augmenting experience data to improve learning stability (Lu et al. 2023). They have also been increasingly applied in high-level decision-making, spanning tasks such as multi-task RL (He et al. 2023), imitation learning (Hegde et al. 2023), and motion trajectory synthesis (Zhang et al. 2024). CD³T builds on these advances by leveraging diffusion models to learn expressive latent representations that capture complex distributional properties, such as skewness and multi-modality—essential for reliable subtask discovery. This enables a more principled and flexible approach to hierarchical decision-making in cooperative MARL.

G. Visualizations

Visual Evidence of Effective Task Decomposition

To further illustrate the reasonableness of CD³T in task decomposition and subtask allocation, we visualize agent trajectories and subtask assignments on the `corridor` scenario across two representative methods. As shown in *Fig. 11(a)*, CD³T maintains a consistently high win rate, underscoring the benefits of its structured decision-making (see Section). Even in the late stage of combat, when only two of six allied agents remain, one agent continues to operate strategically with considerable remaining health. This indicates that the subtask representations learned by CD³T enable robust and context-aware behavior, even under significant pressure of being killed. In contrast, *Fig. 11(b)* reveals clear deficiencies in RODE’s coordination capabilities. Three allied agents act ineffectively from the beginning, with two retreating to a corner and remaining idle for most of the episode. As the remaining agents come under concentrated enemy fire, they display hesitant and uncoordinated movement, failing to provide support or leverage their numerical advantage. As a result, RODE secures only a marginal win, despite an initially favorable position. *Fig. 11(c)* further illustrates the limitations of QMIX, which lacks any discernible tactical structure. Agents engage in an uncoordinated frontal assault and are rapidly eliminated by focused enemy attacks. Although one agent sporadically exhibits basic kiting behavior, the absence of a collective strategy renders such efforts ineffective.

These visualizations highlight the advantage of CD³T’s hierarchical framework, which facilitates clear subtask delineation and consistent coordination. By leveraging diffusion-based representations, agents are able to adapt their roles dynamically and cooperate efficiently, resulting in resilient and strategically sound group behavior.



(a) Visualizations of CD^3T in one episode on corridor.



(b) Visualizations of $RODE$ in one episode on corridor.



(c) Visualizations of $QMIX$ in one episode on corridor.

Figure 11: Qualitative comparison of CD^3T , $RODE$, and $QMIX$ on corridor. Each row depicts a sequence of visualizations from a single episode under the same scenario, illustrating the agent behaviors and coordination patterns exhibited by each method.

Reproducibility Checklist

1. General Paper Structure

- 1.1. Includes a conceptual outline and/or pseudocode description of AI methods introduced (yes/partial/no/NA) **yes**
- 1.2. Clearly delineates statements that are opinions, hypothesis, and speculation from objective facts and results (yes/no) **yes**
- 1.3. Provides well-marked pedagogical references for less-familiar readers to gain background necessary to replicate the paper (yes/no) **yes**

2. Theoretical Contributions

- 2.1. Does this paper make theoretical contributions? (yes/no) **yes**

If yes, please address the following points:

- 2.2. All assumptions and restrictions are stated clearly and formally (yes/partial/no) **yes**
- 2.3. All novel claims are stated formally (e.g., in theorem statements) (yes/partial/no) **yes**
- 2.4. Proofs of all novel claims are included (yes/partial/no) **yes**
- 2.5. Proof sketches or intuitions are given for complex and/or novel results (yes/partial/no) **yes**
- 2.6. Appropriate citations to theoretical tools used are given (yes/partial/no) **yes**
- 2.7. All theoretical claims are demonstrated empirically to hold (yes/partial/no/NA) **yes**
- 2.8. All experimental code used to eliminate or disprove claims is included (yes/no/NA) **NA**

3. Dataset Usage

- 3.1. Does this paper rely on one or more datasets? (yes/no) **no**

If yes, please address the following points:

- 3.2. A motivation is given for why the experiments are conducted on the selected datasets (yes/partial/no/NA) **NA**
- 3.3. All novel datasets introduced in this paper are included in a data appendix (yes/partial/no/NA) **NA**
- 3.4. All novel datasets introduced in this paper will be made publicly available upon publication of the paper with a license that allows free usage for research purposes (yes/partial/no/NA) **NA**
- 3.5. All datasets drawn from the existing literature (potentially including authors' own previously published work) are accompanied by appropriate citations (yes/no/NA) **NA**
- 3.6. All datasets drawn from the existing literature (potentially including authors' own previously published work) are publicly available (yes/partial/no/NA) **NA**
- 3.7. All datasets that are not publicly available are described in detail, with explanation why publicly available alternatives are not scientifically satisfying (yes/partial/no/NA) **NA**

4. Computational Experiments

- 4.1. Does this paper include computational experiments? (yes/no) **yes**

If yes, please address the following points:

- 4.2. This paper states the number and range of values tried per (hyper-) parameter during development of the paper, along with the criterion used for selecting the final parameter setting (yes/partial/no/NA) **yes**
- 4.3. Any code required for pre-processing data is included in the appendix (yes/partial/no) **NA**
- 4.4. All source code required for conducting and analyzing the experiments is included in a code appendix (yes/partial/no) **yes**

- 4.5. All source code required for conducting and analyzing the experiments will be made publicly available upon publication of the paper with a license that allows free usage for research purposes (yes/partial/no) **yes**
- 4.6. All source code implementing new methods have comments detailing the implementation, with references to the paper where each step comes from (yes/partial/no) **yes**
- 4.7. If an algorithm depends on randomness, then the method used for setting seeds is described in a way sufficient to allow replication of results (yes/partial/no/NA) **yes**
- 4.8. This paper specifies the computing infrastructure used for running experiments (hardware and software), including GPU/CPU models; amount of memory; operating system; names and versions of relevant software libraries and frameworks (yes/partial/no) **yes**
- 4.9. This paper formally describes evaluation metrics used and explains the motivation for choosing these metrics (yes/partial/no) **yes**
- 4.10. This paper states the number of algorithm runs used to compute each reported result (yes/no) **yes**
- 4.11. Analysis of experiments goes beyond single-dimensional summaries of performance (e.g., average; median) to include measures of variation, confidence, or other distributional information (yes/no) **yes**
- 4.12. The significance of any improvement or decrease in performance is judged using appropriate statistical tests (e.g., Wilcoxon signed-rank) (yes/partial/no) **yes**
- 4.13. This paper lists all final (hyper-)parameters used for each model/algorithm in the paper's experiments (yes/partial/no/NA) **yes**